Multiscale analysis in solids with unseparated scales: fine-scale recovery, error estimation, and coarse-scale adaptivity

Joseph E. Bishop*

Component Sciences and Mechanics Department,
Engineering Sciences Center,
Sandia National Laboratories,
Albuquerque, NM 87185, USA
Email: jebisho@sandia.gov
*Corresponding author

Judith A. Brown

Fluid and Reactive Processes Department,
Engineering Sciences Center,
Sandia National Laboratories,
Albuquerque, NM 87185, USA
Email: judbrow@sandia.gov

Theron M. Rodgers

Computational Materials and Data Science Department,
Material Sciences Center,
Sandia National Laboratories,
Albuquerque, NM 87185, USA
Email: trodger@sandia.gov

Abstract: There are several engineering applications in which the assumptions of homogenisation and scale separation may be violated, in particular, for metallic structures constructed through additive manufacturing. Instead of resorting to direct numerical simulation of the macroscale system with an embedded fine scale, an alternative approach is to use an approximate macroscale constitutive model, but then estimate the model-form error using *a posteriori* error estimation techniques and subsequently adapt the macroscale model to reduce the error for a given boundary value problem and quantity of interest. We investigate this approach to multiscale analysis in solids with unseparated scales using the example of an additively manufactured metallic structure consisting of a polycrystalline microstructure that is neither periodic nor statistically homogeneous. As a first step to the general nonlinear case, we focus here on linear elasticity in which each grain within the polycrystal is linear elastic but anisotropic.

Keywords: error estimation; model-form error; model adaptivity; uncertainty quantification; additive manufacturing; polycrystal; multiscale.

Biographical notes: Joseph E. Bishop leads a Modelling and Simulation Department within the Engineering Sciences Center at Sandia National Laboratories. He obtained his PhD in Aerospace Engineering at Texas A&M University in 1995 studying the mechanics of composite materials. From 1996 to 2004, he worked in the Synthesis and Analysis Department within the Powertrain Division of General Motors Corporation performing thermal-structural analysis of internal-combustion engines. He joined Sandia National Laboratories in 2004 and has since worked on a variety of research and application projects. His research interests include multiscale modelling, polyhedral finite element formulations, and mesh-free methods.

Judith A. Brown is a member of the Fluid and Reactive Processes Department at Sandia National Laboratories. She holds a PhD degree in Mechanical Engineering from North Carolina State University, where she developed a novel modelling approach to study laser interaction with energetic aggregates. After joining Sandia in 2015, she has used her background in computational solid mechanics and materials science to study heterogeneous material systems through mesoscale modelling with the goal of developing predictive, macroscale constitutive models. Her research interests include multiphysics and multiscale modelling, energetic materials in extreme environments, particulate composites, and foams.

Theron M. Rodgers is a member of the Computational Materials Science Department at Sandia National Laboratories. He joined the department as a postdoc in 2015 after completing his PhD in Engineering Physics at the University of Virginia. His research focuses on simulating microstructure formation during advanced manufacturing, microstructure quantification, and the use of microstructures in engineering analyses. He has developed simulation methods for several processing techniques including vapour deposition, welding, plasma spray, cold spray, and additive manufacturing. He has coauthored over 18 journal articles and released multiple applications in the open source SPPARKS repository.

1   Introduction

In engineering practice, modelling the macroscale response of a structure requires the use of a material constitutive model that approximates the effective behaviour of the underlying material microstructure over a desired range of loading conditions. However, in many cases a macroscale material model is only an approximation to the true response of the material, especially in regimes of loading that differ significantly from the calibration regime. There are also fundamental limitations in defining an effective or homogenised material, in particular for materials whose microstructure is neither periodic nor statistically homogeneous. Typical examples include welded regions of a metallic structure, structures resulting from a casting process or metal additive manufacturing (AM), and certain composite material systems. Furthermore, typical structures possess

numerous stress concentrations that can invalidate the separation-of-scales assumption when local stress gradients occur on the same length scale as the material grains or individual constituents of a composite. For these examples, there is no longer a clear demarcation of 'material' with well-defined properties and the structural system comprised of the material; rather, features and properties of the local microstructure will determine the behaviour.

Figure 1   Grain morphology and crystal orientation of 304L stainless steel, (a) wrought material (b) AM material (see online version for colours)

(a)

(b)
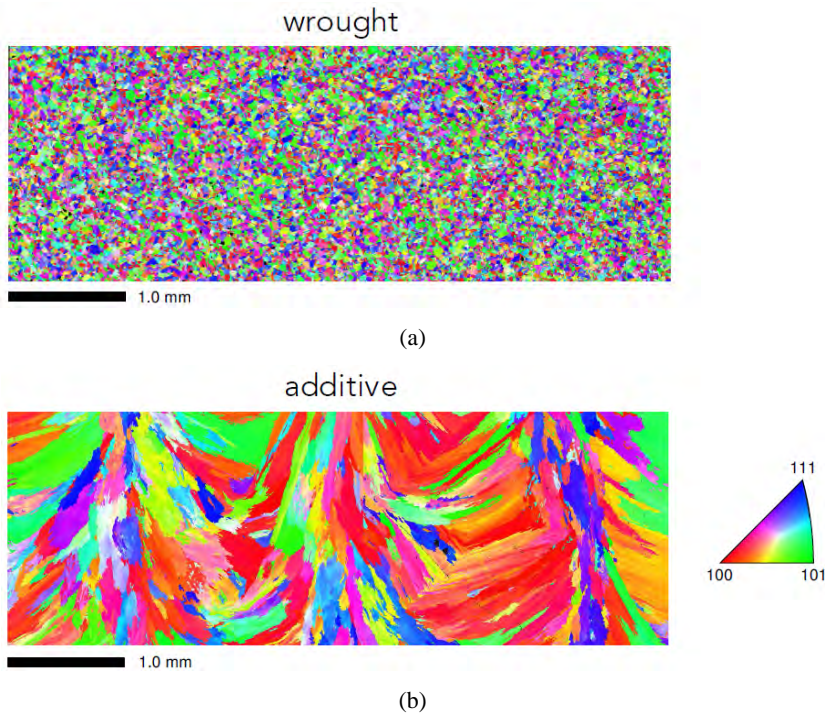
Note: Reproduced with permission from Bishop and Brown (2018).

Our motivation for this work is the quantification of model-form errors present in the simulation of AM structures (Adams et al., 2019; Johnson et al., 2018; Li et al., 2010; Denlinger et al., 2014; Pal et al., 2014; Markl and Körner, 2016; Smith et al., 2016). Due to the nature of the manufacturing process, these materials may not possess a separation-of-scales. This makes the use of homogenisation (Cioranescu and Donato, 1999; Zohdi and Wriggers, 2008; Christensen, 2005; Torquato, 2002), e.g., through representative volume elements (Kanit et al., 2003) or self-consistent methods (Lebensohn and Tomé, 1993; Yaguchi and Busso, 2005; Wang et al., 2010), an approximation (Bishop et al., 2015, 2016). An example material microstructure for stainless steel resulting from a laser engineered net shaping (LENS) process (Griffith et al., 1996; Adams et al., 2019) is shown in Figure 1. The microstructure of a traditional wrought material is shown for comparison. The materials/structures resulting from AM can exhibit significant polycrystalline texture, even by design (Dinda et al., 2012; Antonysamy et al., 2013; Parimi et al., 2014; Dehoff et al., 2015; Wei et al., 2016). Thus,

the typical assumption of mechanical isotropy in these materials is an approximation whose error must be quantified (Hendrix and Yu, 1998; Tang and Pistorius, 2017). Similar types of errors exist in the macroscale representation of welds (Bouche et al., 2000; Unnikrishnan et al., 2014; Brown and Bishop, 2019), composite materials (Christensen, 2005), random heterogeneous media (Torquato, 2002; Zohdi and Wriggers, 2008), and whenever approximate material models are used at the macroscale.

If a sufficiently accurate representation of the fine-scale microstructure existed, along with an appropriate constitutive model at the fine scale, direct numerical simulation could be used to model the macroscale response of a structure comprised of unseparated scales (Bishop et al., 2015, 2016; Rodgers et al., 2018). However, given current computing resources, this approach is clearly not tenable for most engineering structures, even if using an optimal geometric multigrid solver with computational complexity $O(N)$, where N is the number of degrees of freedom in the model (Yushu and Matouš, 2020; Liu et al., 2020; Miehe and Bayreuther, 2007). An alternative approach is to seek an approximate macroscale solution and then quantify the error or uncertainty in the solution using techniques from the field of *multiscale* model-form a *posteriori* error estimation. The resulting model-form error is in addition to the discretisation error. In this approach, the approximate coarse-scale (macroscale) model is solved first, followed by an *offline* recovery of an approximate fine-scale solution through one of several methods. The model-form error can then be assessed using both the solution to the approximate coarse-scale model and the recovered fine-scale solution. This methodology has been developed extensively in both single and multiscale contexts by Oden and collaborators (Zohdi et al., 1996; Oden and Zohdi, 1997; Moës et al., 1998; Oden and Vemaganti, 1999; Oden et al., 1999; Oden and Vemaganti, 2000; Vemaganti and Oden, 2001; Oden et al., 2001; Romkes et al., 2006). Recently, this model-form *a posteriori* error estimation methodology has been used to assess the *single* scale error in simplified representations of welded and AM structures (Bishop and Brown, 2018; Brown and Bishop, 2019). In this work, we investigate the *multiscale* error-estimation methodology using an example of an AM metallic structure consisting of a polycrystalline microstructure that is neither periodic nor statistically homogeneous. The AM microstructure is realised using a kinetic Monte-Carlo (KMC) methodology (Rodgers et al., 2018). A traditional wrought microstructure with equiaxed grains is also used for comparison. The wrought microstructure is statistically homogeneous and readily homogenisable using standard techniques. Several methods are investigated for recovering the fine-scale fields, given the coarse-scale solution.

Once a local-error indicator is obtained for the approximate macroscale solution, the error may be reduced through various adaptive techniques. Previous approaches for reducing the modelling error have emphasised replacing the less accurate macroscale material model with the true microstructural model in regions where the local-error indicators were relatively large (Oden and Zohdi, 1997; Oden and Vemaganti, 1999, 2000; Vemaganti and Oden, 2001; Oden et al., 2001). In contradistinction, we reduce the modelling error by adapting the material parameters in the approximate macroscale constitutive model. These adapted parameters may vary spatially.

Although we are ultimately interested in assessing errors in engineering quantities of interest (Oden and Vemaganti, 2000; Vemaganti and Oden, 2001), in this work, we focus only on error assessments in the energy norm. As a first step to nonlinear boundary-value problems (Oden et al., 2001; Larsson and Runesson, 2004, 2006, 2008), we consider here only linear elasticity. Section 2 reviews linear elasticity, establishing notation and

solution norms, and provides a short note on homogenisation theory. Section 3 reviews the multiscale error-estimation framework. Several methods for recovering the fine-scale solution from an approximate macroscale solution are given in Section 4. Section 5 provides a detailed example demonstrating the fine-scale recovery process and the multiscale error estimation process for a synthetic AM structure. An algorithm for adapting the macroscale material parameters and reducing the model-form error is given in Section 6. A summary is provided in Section 7. Key equations are included in a box for clarity throughout the text.

2   Problem formulation

In this section, we review the governing equations for linear elasticity, define several solution norms, and provide a short note on homogenisation theory.

2.1   Governing equations

Consider a body $\mathcal{B}$ with boundary Γ and interior Ω. The body is subjected to surface tractions $\mathbf{t}$ per unit area. The position of a material point in the original configuration is denoted by $\mathbf{X}$ and in the current configuration by $\mathbf{x}$. The displacement vector $\mathbf{u}$ is given by $\mathbf{u} := \mathbf{x} - \mathbf{X}$. In the absence of body forces, static equilibrium is governed by the vector equation

$$\frac{\partial \boldsymbol{\sigma}}{\partial \mathbf{x}} : \mathbf{I} = \mathbf{0} \tag{1}$$

with boundary conditions

$$\mathbf{u} = \bar{\mathbf{u}} \text{ on } \Gamma_{\mathbf{u}} \text{ and } \boldsymbol{\sigma}\mathbf{n} = \mathbf{t} \text{ on } \Gamma_{\mathbf{t}} \tag{2}$$

Here, $\boldsymbol{\sigma}$ is the Cauchy stress tensor, $\mathbf{I}$ is the identity tensor, n is the outward unit normal on $\Gamma_{\mathbf{t}}$, $\overline{\Gamma_{\mathbf{u}} \cup \Gamma_{\mathbf{t}}} = \Gamma$ and $\Gamma_{\mathbf{u}} \cap \Gamma_{\mathbf{t}} = \varnothing$. Along with vector notation, indicial notation is also used. For example, $\boldsymbol{\sigma}$ is written as σ_{ij} with subscripts $i, j = 1, 2, 3$. Summation is implied on repeated indices unless otherwise noted. For example, $\boldsymbol{\sigma}\mathbf{n} = \sigma_{ij}n_j$ and $\boldsymbol{\sigma}: \boldsymbol{\sigma} = \sigma_{ij}\sigma_{ij}$.

2.2   Linear elasticity

For linear elastic materials, $\sigma = \mathbb{C}\epsilon$, where $\epsilon := sym(\nabla\mathbf{u})$ is the linear strain tensor, and $\mathbb{C}$ is the fourth-order stiffness tensor. For heterogeneous bodies, $\mathbb{C}$ will be spatially varying. We assume that $\mathbb{C}$ satisfies the uniform ellipticity conditions

$$\exists \alpha_l, \alpha_u > 0 \text{ such that } \alpha_l \epsilon : \epsilon \leq \epsilon : (\mathbb{C}(\mathbf{x})\epsilon) \leq \alpha_u \epsilon : \epsilon \quad \forall \epsilon \tag{3}$$

for almost every $\mathbf{x} \in \Omega$. The inverse of $\mathbb{C}$ is the compliance tensor $\mathbb{S} = \mathbb{C}^{-1}$.

Due to the major and minor symmetries of $\mathbb{C}$, there exist only 21 independent elastic constants for general anisotropy. For cubic symmetry, there are three independent elastic constants whereas for an isotropic material there are only two (Bower, 2010). The example problem presented in Section 5 considers a polycrystalline material in which each grain possesses a cubic symmetry with a crystal orientation distribution that is

uniformly random and thus has no preferred orientation (no texture). The approximate macroscale material model for the example is taken to be isotropic and homogeneous.

For isotropic materials, there are only two independent elastic constants, the shear modulus μ and the bulk modulus K. In this special case, the stiffness tensor may be written in the form (Moakher and Norris, 2006),

$$\mathbb{C}^{iso} = (3K)\mathbb{J} + (2\mu)\mathbb{K}. \tag{4}$$

Here, $\mathbb{J}$ and $\mathbb{K}$ are fourth-order tensors defined as

$$(\mathbb{J})_{ijkl} = \frac{1}{3}\delta_{ij}\delta_{kl} \text{ and } \mathbb{K} = \mathbb{I} - \mathbb{J} \tag{5}$$

where $(\mathbb{I})_{ijkl} = \frac{1}{2}(\delta_{ij}\delta_{jl} + \delta_{il}\delta_{jk})$ is the fourth-order identity tensor and δ_{ij} is the second order identity tensor (Kronecker delta). The tensor $\mathbb{J}$ returns the hydrostatic portion of a symmetric second-order tensor, while $\mathbb{K}$ returns the deviatoric,

$$(\mathbb{J}\boldsymbol{\epsilon})_{ij} = \frac{1}{3}\epsilon_{kk}\delta_{ij} \text{ and } (\mathbb{K}\boldsymbol{\epsilon})_{ij} = \epsilon_{ij} - \frac{1}{3}\epsilon_{kk}\delta_{ij} \tag{6}$$

with $\mathbb{J} + \mathbb{K} = \mathbb{I}$. Additionally, $\mathbb{J}$ and $\mathbb{K}$ possess the multiplicative properties $\mathbb{J}\mathbb{J} = \mathbb{J}$, $\mathbb{K}\mathbb{K} = \mathbb{K}$, and $\mathbb{J}\mathbb{K} = \mathbb{K}\mathbb{J} = \mathbb{O}$, where $\mathbb{O}$ is the fourth-order zero tensor. Further properties of these tensors are described in Moakher and Norris (2006). Using these properties, the inverse of equation (4) is simply

$$\mathbb{S}^{iso} = \frac{1}{3K}\mathbb{J} + \frac{1}{2\mu}\mathbb{K}. \tag{7}$$

Note that $\mathbb{C}^{iso}\mathbb{S}^{iso} = \mathbb{S}^{iso}\mathbb{C}^{iso} = \mathbb{J} + \mathbb{K} = \mathbb{I}$.

2.3 Weak form and solution norms

The weak form of equation (1) is given by the following variational problem (Ciarlet, 2002; Bonet and Wood, 2008): find the trial functions $\mathbf{u} \in \mathbf{H}^1(\Omega)$, where $\mathbf{H}^1(\Omega) := [H^1(\Omega)]^3$, with $\mathbf{u} = \bar{\mathbf{u}}$ on $\Gamma_{\mathbf{u}}$ such that

$$\int_{\Omega} \boldsymbol{\sigma} : (\partial\mathbf{v}/\partial\mathbf{x})\,d\Omega = \int_{\Omega} \mathbf{f}\cdot\mathbf{v}\,d\Omega + \int_{\Gamma_{\mathbf{t}}} \mathbf{t}\cdot\mathbf{v}\,d\Gamma \tag{8}$$

for all test functions $\mathbf{v} \in \mathbf{H}_0^1(\Omega)$. Here, $H^1(\Omega)$ is the Sobolev function space of degree one containing functions that possess square-integrable weak derivatives, and the Sobolev space $\mathbf{H}_0^1(\Omega) := \{\mathbf{v} \in \mathbf{H}^1(\Omega) : \mathbf{v} = 0 \text{ on } \Gamma_{\mathbf{u}}\}$. With the assumption of uniform ellipticity for $\mathbb{C}$ in equation (3) and the assumption of regularity of the domain boundary Γ provided by Lipshitz continuity, a unique solution of equation (8) exists (Ciarlet, 2002). Numerical approximations to this solution will be obtained using a standard displacement-based finite element method (Hughes, 2000).

For the linear elastic system of interest here, from equation (8) we can identify the symmetric bilinear form $B(\mathbf{u}, \mathbf{v})$,

$$B(\mathbf{u}, \mathbf{v}) := \int_{\Omega} (\partial \mathbf{u}/\partial \mathbf{x}) : (\mathbb{C}(\partial \mathbf{v}/\partial \mathbf{x})) \, d\Omega \tag{9}$$

and the linear form $F(\mathbf{v})$ as

$$F(\mathbf{v}) := \int_{\Omega} \mathbf{f} \cdot \mathbf{v} \, d\Omega + \int_{\Gamma_{\mathbf{t}}} \mathbf{t} \cdot \mathbf{v} \, d\Gamma. \tag{10}$$

Thus, the variational boundary value problem becomes: find the trial functions $\mathbf{u} \in \mathbf{H}^1(\Omega)$ with $\mathbf{u} = \bar{\mathbf{u}}$ on $\Gamma_{\mathbf{u}}$ such that

$$B(\mathbf{u}, \mathbf{v}) = F(\mathbf{v}) \tag{11}$$

for all test functions $\mathbf{v} \in \mathbf{H}_0^1(\Omega)$. We also define the potential energy functional Π of the system as

$$\Pi(\mathbf{w}) := \frac{1}{2} B(\mathbf{w}, \mathbf{w}) - F(\mathbf{w}). \tag{12}$$

The energy norm (natural norm) $\|\cdot\|_E$ of $\mathbf{u}$ is given by,

$$\|\mathbf{u}\|_E := \sqrt{B(\mathbf{u}, \mathbf{u})} = \left(\int_{\Omega} \boldsymbol{\epsilon} : (\mathbb{C}\boldsymbol{\epsilon}) \, d\Omega \right)^{1/2} \tag{13}$$

where $\mathbf{u}$ represents a kinematically admissible displacement field within $\mathbf{H}^1(\Omega)$ so that $\|\mathbf{u}\|_E = 0$ implies $\mathbf{u} = 0$ almost everywhere. The Frobenius norm of a second-order tensor σ at a given material point is defined as

$$\|\boldsymbol{\sigma}\| := \sqrt{\boldsymbol{\sigma} : \boldsymbol{\sigma}} = \sqrt{\sigma_{ij} \sigma_{ij}}. \tag{14}$$

Similarly, for a second-order tensor field $\boldsymbol{\sigma}(\mathbf{x})$, the norm is defined as

$$\|\boldsymbol{\sigma}\|_{\Omega} := \left(\int_{\Omega} \boldsymbol{\sigma}(\mathbf{x}) : \boldsymbol{\sigma}(\mathbf{x}) \, d\Omega \right)^{1/2} = \left(\int_{\Omega} \sigma_{ij}(\mathbf{x}) \sigma_{ij}(\mathbf{x}) \, d\Omega \right)^{1/2}. \tag{15}$$

2.4   Note on material homogenisation

Homogenisation is the process of substituting a heterogeneous material with a fictitious homogeneous material whose macroscale response is energetically equal to that of the true heterogeneous material (Cioranescu and Donato, 1999; Bishop and Lim, 2016). The resulting properties of the fictitious homogeneous material are called the *effective* or homogenised material properties (Huet, 1990). These properties are well defined (they exist and are unique) if the microstructure is either periodic or statistically homogeneous (Cioranescu and Donato, 1999; Tran et al., 2012; Jikov et al., 1994; Bensoussan et al., 2011). Note that the effective properties are deterministic, even for random microstructures (Papanicolaou and Varadhan, 1979). Their use in a boundary value problem implicitly assumes that there is a 'scale separation' in which the microstructural length scale is infinitesimally small compared to those of the macroscale problem. When the necessary conditions for material homogenisation do not exist within a material, then the sampled material properties are referred to as *apparent* material properties by Huet (1990). Their use in a boundary value problem merely provides an approximation of the

true structural response, although a very good approximation for conventional engineering materials.

Homogenisation theory provides the fundamental result that the displacement field of the macroscopic boundary value problem containing the true heterogeneous material converges *strongly* to the displacement field of the macroscopic boundary value problem containing the homogenised material (Cioranescu and Donato, 1999). However, the stress and strain fields of the macroscopic boundary value problem containing the heterogeneous material converge only *weakly*. Equivalent results hold for random microstructures using probabilistic definitions of convergence (Papanicolaou and Varadhan, 1979). If the assumptions of homogenisation theory hold, then the fine-scale solution can be recovered in a post-processing step (localisation or submodelling) (Cioranescu and Donato, 1999).

For finite periodic microstructures, additional terms arise in the balance of linear momentum for a finite microstructure. These additional terms involved gradients of strain (Tran et al., 2012; Boutin, 1996; Yuan et al., 2008; Smyshlyaev and Cherednichenko, 2000), and higher-order material properties exist as well. Surface effects on the order of the microstructural length scale also exist for both periodic and random microstructures (Auriault and Bonnet, 1987; Dumontet, 1987).

For AM metallic structures, the microstructure is neither periodic nor statistically homogeneous (see Figure 1, for example). Thus, there is not a well defined effective medium. Questions then arise regarding the magnitude of the error induced in macroscale quantities of interest by using an approximate effective material. The accuracy of homogenisation theory for structures containing finite polycrystalline microstructures has been studied using direct numerical simulations in both the elastic and plastic regimes by Bishop et al. (2015, 2016), respectively, and for synthetic AM structures by Rodgers et al. (2018). Generalised finite element methods could also be used to efficiently solve for the fine-scale solution by using a multiscale finite element basis derived using *a priori* computed local solutions (Chamoin and Legoll, 2021; Målqvist and Peterseim, 2021; Efendiev and Hou, 2009; Strouboulis et al., 2001).

3   Estimation of multiscale material model-form error

Let **u** represent the exact displacement from equation (1) based on the true heterogeneous microscale stiffness tensor $\mathbb{C}(\mathbf{x})$. In typical applications, this solution is computationally intractable by direct simulation or through conventional homogenisation techniques. Instead, an approximate solution is obtained by solving an approximate boundary-value problem, thus inducing an error. We seek to bound this induced error. To this goal, an approximate macroscale material model is used with stiffness tensor $\mathbb{C}^0$, possibly spatially varying but with a length scale much larger than that of the fine scale. The associated displacement solution is denoted by $\mathbf{u}^0$ with associated stress $\boldsymbol{\sigma}^0$ and strain $\boldsymbol{\epsilon}^0$ fields.

The total approximation error e may be decomposed into contributions from the model form error $\mathbf{e}^{\text{model}}$ and the discretisation error $\mathbf{e}^{0,h}$ of the coarse scale boundary-value problem,

$$\mathbf{e} = \mathbf{e}^{\text{model}} + \mathbf{e}^{0,h}. \tag{16}$$

The modelling error $\mathbf{e}^{\text{model}}$ is given by

$$\mathbf{e}^{\text{model}} := \mathbf{u} - \mathbf{u}^0. \tag{17}$$

The finite element method is used to obtain a discrete solution of the approximate macroscale boundary-value problem. This discrete solution is denoted by $\mathbf{u}^{0,h}$, where h denotes the element size. The discretisation error of this approximate boundary-value problem is given by

$$\mathbf{e}^{0,h} := \mathbf{u}^0 - \mathbf{u}^{0,h}. \tag{18}$$

The total approximation error $\mathbf{e}$ is then

$$\mathbf{e} := \mathbf{u} - \mathbf{u}^{0,h}. \tag{19}$$

An application of the triangle-inequality property of norms gives

$$\|\mathbf{e}\|_E = \|\mathbf{e}^{\text{model}} + \mathbf{e}^{0,h}\|_E \leq \|\mathbf{e}^{\text{model}}\|_E + \|\mathbf{e}^{0,h}\|_E. \tag{20}$$

In practice, either the modelling error or the discretisation error can dominate the total error. The model-form error $\mathbf{e}^{\text{model}}$ is our primary concern. Thus, we assume through the use of highly refined discretisations that $\|\mathbf{e}^{0,h}\|_E << \|\mathbf{e}^{\text{model}}\|_E$.

The primary objective of *a posteriori* error estimation is to estimate, and preferably bound, the solution error using the approximate solution, here $\mathbf{u}^0$. The following bound on $\|\mathbf{e}^{\text{model}}\|_E$ has been obtained by Zohdi et al. (1996),

$$\|\mathbf{e}^{\text{model}}\|_E^2 \leq \int_\Omega (\epsilon^0 - \mathbb{S}\boldsymbol{\sigma}^0):(\mathbb{C}\epsilon^0 - \boldsymbol{\sigma}^0)\,d\Omega. \tag{21}$$

Note that this bound uses the known quantities, $\boldsymbol{\sigma}^0$, ϵ^0, and $\mathbb{C}$. Since the integrand in equation (21) is non-negative, a local error *indicator*, denoted by ζ is defined as

$$\boxed{\zeta^2 := (\epsilon^0 - \mathbb{S}\boldsymbol{\sigma}^0):(\mathbb{C}\epsilon^0 - \boldsymbol{\sigma}^0)} \tag{22}$$

The bound is then given by

$$Z^2 := \int_\Omega \zeta^2 d\Omega \tag{23}$$

so that

$$\|\mathbf{e}^{\text{model}}\|_E^2 \leq Z^2. \tag{24}$$

We may partition Ω into a finite number of subdomains Ω_M, $M = 1, 2, \ldots, N$. Then, Z^2 in equation (23) may be written as

$$Z^2 = \sum_{M=1}^{N} Z_M^2 \tag{25}$$

where

$$Z_M^2 \doteq \int_{\Omega_M} \zeta^2 d\Omega_M \tag{26}$$

is the contribution of subregion M to the error bound. Due to pollution effects, the local-error indicator ζ can be small while the local error is still large (Ainsworth and Oden, 2011). The energy norm of the error field is bounded in equation (24), but not the local point-wise error. For example, ζ is identically zero if $\mathbb{C}^0 = \mathbb{C}$ locally.

Figure 2　Partition of a domain into subdomains and definition of patches for use in the fine-scale recovery process, (a) example domain of a hole in a plate (b) partition of the domain into subdomains using a standard quadrilateral mesh (c) definition of three types of patches (see online version for colours)
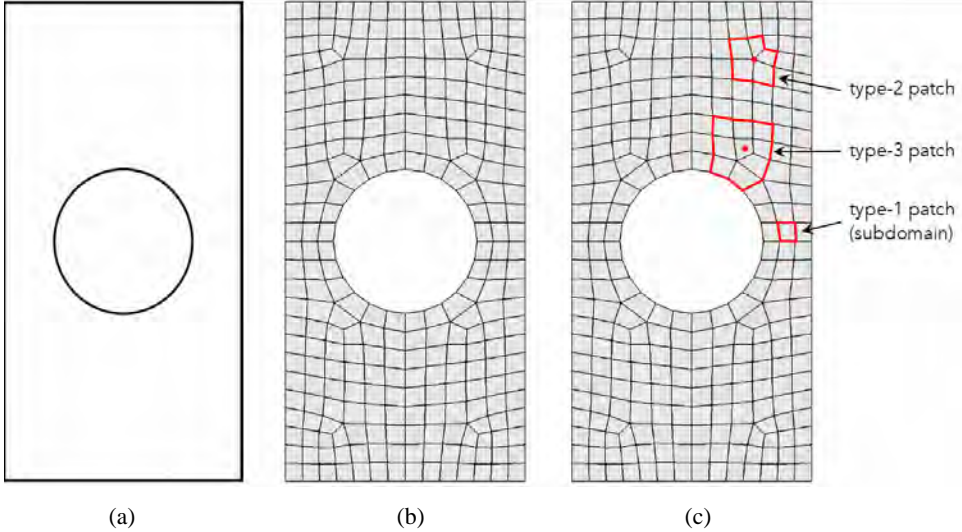
Notes: A type-1 patch is simply a subdomain. A type-2 patch is the union of the subdomains attached to a subdomain vertex. A type-3 patch is the union of subdomains attached to a given subdomain.

The model-form *a posteriori* error bound given by equation (21) has been used recently to assess the *single* scale error in simplified representations of welded and AM structures (Bishop and Brown, 2018; Brown and Bishop, 2019). However, as noted by Brown and Bishop (2019), the bound can become too conservative in the case of multiscale analysis due to the fluctuating stress and strain fields at the fine scale. Oden and Zohdi (1997) proposed a tighter bound that requires the recovery of an approximate fine-scale solution, denoted here by $\mathbf{w}$, using the coarse-scale approximation $\mathbf{u}^0$. To establish this bound, note that for any kinematically admissible $\mathbf{w}$

$$\|\mathbf{w} - \mathbf{u}\|_E^2 = 2\left(\Pi(\mathbf{w}) - \Pi(\mathbf{u})\right) \tag{27}$$

which can be derived using the definition of Π given in equation (12), noting the identity $\|w - u\|_E^2 = B(\mathbf{w} - \mathbf{u}, \mathbf{w} - \mathbf{u})$, and using equation (11) noting that $\mathbf{w} - \mathbf{u} \in \mathbf{H}_0^1(\Omega)$. Using equation (27) and noting that $\mathbf{u}^0$ is kinematically admissible, we have

$$\Pi(\mathbf{w}) - \Pi(\mathbf{u}^0) = \Pi(\mathbf{w}) - \Pi(\mathbf{u}) + \Pi(\mathbf{u}) - \Pi(\mathbf{u}^0) = \frac{1}{2}\|\mathbf{w} - \mathbf{u}\|_E^2 - \frac{1}{2}\|\mathbf{u}^0 - \mathbf{u}\|_E^2 \tag{28}$$

so that

$$\|\mathbf{w}-\mathbf{u}\|_E^2 = 2\left(\prod(\mathbf{w})-\prod(\mathbf{u}^0)\right)+\|\mathbf{u}^0-\mathbf{u}\|_E^2. \tag{29}$$

The last term on the right can be bounded using equation (21) resulting in

$$\|\mathbf{w}-\mathbf{u}\|_E^2 \le 2\left(\prod(\mathbf{w})-\prod(\mathbf{u}^0)\right)+Z^2. \tag{30}$$

This bound uses only known (computable) quantities. Note that the fine-scale approximation $\mathbf{w}$ is more accurate than coarse scale approximation $\mathbf{u}^0$ in the fine-scale energy functional $\prod$. Thus, we expect that $\prod(\mathbf{w}) < \prod(\mathbf{u}^0)$ so that equation (30) is a tighter bound than just using equation (24) alone. Unfortunately, it is not as straight forward to identify a local-error indicator as with ζ^2 in equation (22). Finally, define β^2 as the negative of the first term in the right hand side of equation (30),

$$\beta^2 := 2\left(\prod(\mathbf{u})^0-\prod(\mathbf{w})\right) \tag{31}$$

so that equation (30) becomes

$$\boxed{\|\mathbf{w}-\mathbf{u}\|_E^2 \le Z^2-\beta^2 := \psi^2}. \tag{32}$$

4   Localisation (submodelling)

In order to use the error bound in equation (32), we need to recover a fine-scale approximation $\mathbf{w} \in \mathbf{H}^1(\Omega)$ that is kinematically admissible. This recovery is similar to the localisation process in homogenisation theory or submodelling in commercial finite element software, e.g., Abaqus (2021). We first partition the domain Ω into a set of simply connected open subsets (subdomains) $\{\Omega_M, M = 1, \ldots, N_S\}$ as shown in Figure 2 such that,

$$\overline{\Omega} = \cup_{M=1}^{N_S}\overline{\Omega}_M \tag{33}$$

where $\overline{\Omega}$ denotes the closure of the domain Ω. Each local subdomain Ω_M is then discretised with a fine-scale mesh to resolve the microstructure. Local patches of subdomains are then formed by combining several subdomains as described below. Appropriate boundary conditions inherited from the approximate coarse-scale solution $\mathbf{u}^0$ will then be applied to the boundary of each patch. The local solutions obtained within each patch are then combined to obtain a continuous and kinematically admissible displacement field $\mathbf{w}$.

There are several possibilities for defining boundary conditions for each patch. We could prescribe $\mathbf{u}^0$ independently to each patch boundary and then use a partition of unity [e.g., using the coarse-scale finite element basis or using reproducing kernel methods (Chen et al., 2017)] to construct a continuous and kinematically admissible displacement field. This approach has the advantage that the solution on each patch is independent of the other patches and thus perfectly parallel. Alternatively, a *sequential* recovery approach can be used by first partitioning the set of patches into disjoint subsets. This sequencing of patches can be obtained using any of a variety of graph colouring algorithms (Lewis, 2016). The first subset of patches in the sequence gets boundary conditions directly from $\mathbf{u}^0$. Each subset of patches in the sequence inherits the boundary

conditions from the combined solution of the previous set of patches. In this way, a compatible and kinematically admissible displacement field is obtained for each step in the sequence. The final step in the sequence provides **w**. This approach is used herein.

For the example presented in Section 5, we compare three sequential recovery methods distinguished by the amount of overlap in the patches. These three recovery methods will be referred to as *type-1*, *type-2*, and *type-3* and are illustrated in Figure 2(c). Type-1 recovery is the special case in which each patch consists of only one subdomain and there is no overlap between the patches. For this case, $\mathbf{u}^0$ is applied independently to each subdomain Ω_M. This recovery method is also referred to as the homogeneous Dirichlet projection method (HDPM) by Zohdi et al. (1996). This recovery process is embarrassingly parallel, but is expected to be the least accurate of the three recovery methods studied here.

Type-2 and type-3 recovery methods entail constructing a set of *overlapping* patches. For type-2 recovery, each patch is formed by taking the union of subdomains connected to a vertex of the initial partition. For type-3 recovery, each patch is formed by taking the union of subdomains connected to a given subdomain of the initial partition. Thus, the patches are increasingly larger in progressing from type-1 recovery to type-3 recovery. We expect the recovered local solution **w** to be more accurate the larger the patch size, but also more computationally expensive. Of course, the patch size also depends on the size of the initial partition. In the limit of a patch size becoming the size of the original domain Ω then the recovery process becomes the original fine-scale problem. Note that type-2 and type-3 recovery methods can be viewed as one iteration within a domain-decomposition iterative solver (Dolean et al., 2015). Additional iterations could be performed to recover increasingly more accurate fine-scale solutions. These recovery methods can also be viewed as a prolongation step within a multigrid method (Briggs et al., 2000).

For type-2 and type-3 recovery methods, several types of graph colouring schemes can be used. The use of an optimisation-based colouring scheme would minimise the number of steps in the sequential recovery sequence. Here, however, we use the simple greedy algorithm that is not necessarily optimal (Lewis, 2016). Also, with a greedy algorithm the recovery sequence will depend on the ordering of the initial subdomains. The number of patches and length of the recovery sequence for each type of recovery method is given in Section 5 for the presented example problem. The type-2 and type-3 recovery methods are sequentially parallel, unlike type-1 which is perfectly parallel.

5   Example

We present an example demonstrating the fine-scale solution recovery and multiscale *a posteriori* error estimation in the energy norm. The boundary-value problem consists of a small tube subjected to tension. Two holes are present on the side of the tube. Subsection 5.1 describes the geometry and boundary conditions. The material is chosen to be AISI 304L stainless steel. Error estimation results are obtained as described in Subsection 5.2 by considering two different types of microstructure as the reference or 'exact' material. The first is an idealised equiaxed microstructure obtained through a special type of Voronoi tessellation (Bishop et al., 2015, 2016). The second microstructure results from a simulated laser-based AM process. This AM microstructure is obtained through a KMC process (Rodgers et al., 2018). The partition of the tube into

subdomains is described in Subsection 5.3. The fine-scale recovery process is given in Subsection 5.4. Additionally, the exact solution with each microstructure is computed via direct numerical simulation and used to calculate the exact error for the approximate solutions obtained with each recovery method. Error estimates are given in Subsection 5.5.

Figure 3 Dimensions of the tube with two side holes used in the example problem
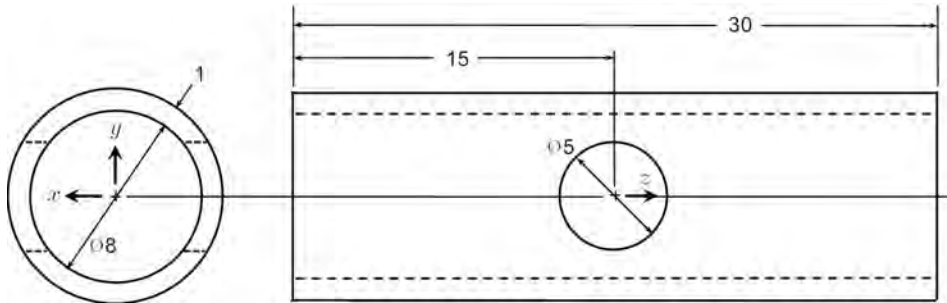
Note: Reproduced with permission from Bishop and Brown (2018).

Figure 4 Isometric view of the example geometry, a tube with two side holes (see online version for colours)
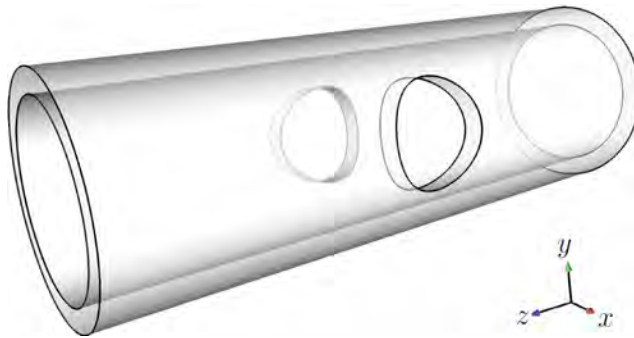

The approximate macroscale material model for each of the studied microstructures is chosen to be homogeneous and isotropic with Young's modulus $E = 197.5$GPa and Poisson's ratio $v = 0.294$. These values are the true homogenised values for the equiaxed Voronoi microstructure in the limit of infinitesimally small grain size and no texture (Bishop et al., 2015). The finite-element software Sierra (Shaw et al., 2017) was used for the simulations. The Sierra software is massively parallel, allowing for a brute-force calculation of the exact solution and assessment of the true error. Special-purpose software was developed to setup the local patch boundary-value problems, run the simulations, and to combine the individual results from each patch into a global fine-scale approximation **w**.

5.1 Tube geometry, boundary conditions, and coarse-scale solution

The dimensions of the tube are shown in Figure 3, and an $(x\ y\ z)$ coordinate system is identified. The dimension units are millimetres (mm) so that the stress/traction units are

megapascals (MPa). Figure 4 shows a three-dimensional view of the tube. The software Cubit (2021) was used to create both the geometry, domain partition, and hexahedral mesh of each subdomain. The partition and fine-scale finite element discretisation are described in Subsection 5.3. The full finite element model consists of 29.8 M hexahedral elements with 32 elements through the thickness of the tube. This full model is used to obtain the *exact* fine-scale solution with embedded microstructure. For simplicity, this same mesh is also used to calculate the macroscale solution using the approximate material model, although a much coarser mesh could be used in practice.

Figure 5   von Mises stress field in the tube with side holes subjected to uniaxial tractions at the ends using a homogeneous and isotropic elastic material model (units are MPa) (see online version for colours)
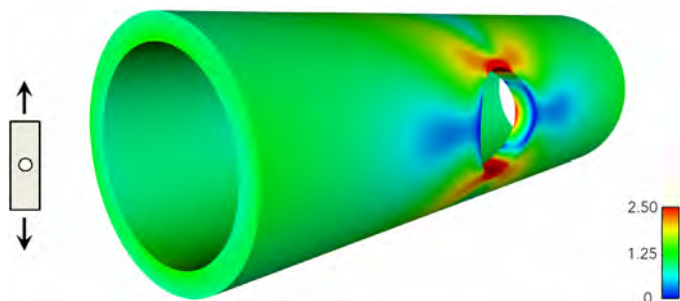
Unit normal tractions of 1 MPa (tension) are applied to the surface of the tube at $z = 15$ and $z = -15$. Minimal displacement boundary conditions are given in order to prevent rigid body motion. The resulting von Mises stress field in the tube is shown in Figure 5 for the homogeneous and isotropic elastic material model with Young's modulus $E = 197.5$ GPa and a Poisson's ratio $v = 0.294$. Note the stress concentration and stress gradients around the side holes, as expected.
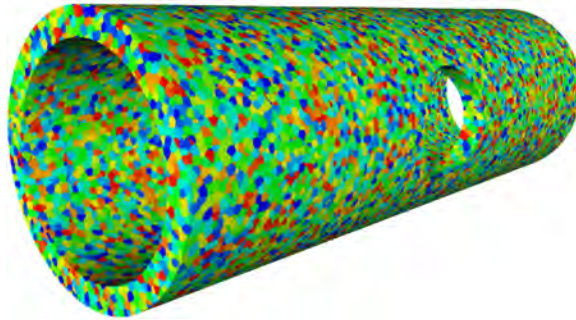
5.2   *Microstructure*

Fine-scale recovery and error bounds are presented for two types of microstructure for the 304L stainless steel material:

1   equiaxed (equal axes) polycrystalline microstructure representative of traditional wrought materials

2   a non-equiaxed irregular polycrystalline microstructure modelled after the LENS AM process (see Figure 1).

For both cases, the crystal structure of each grain is austenitic (γ-Fe) with a face-centred cubic (FCC) crystal system and three independent elastic constants $C_{11} = 205$ GPa, $C_{12} = 138$ GPa, and $C_{44} = 126$ GPa (Ledbetter, 1984). The anisotropy ratio A for this crystal is $A = 2C_{44} / (C_{11} - C_{12}) = 3.8$, which is relatively large. For an isotropic material, $A = 1$. For simplicity, the three dimensional orientation distribution of the grains is taken to be uniformly random (no preferred orientation and texture). This is a reasonable approximation for a wrought material, but much less so for an additive material (Brown and Bishop, 2019). Thus, only grain size, morphology, and spatial distribution differentiates the two cases, wrought and additive.

Figure 6 Tube with imprinted equiaxed grain structure induced by an overlayed Voronoi tessellation (see online version for colours)

Notes: The number of grains is 51 750 with approximately four grains through the tube thickness (grain colouring is random).

5.2.1 *Wrought microstructure*

For the wrought microstructure, a Voronoi tessellation with a specific cell seeding resulting in equiaxed Voronoi cells is used to define the grains. The Voronoi seeding is a random close packing realised through a maximal Poisson sampling as described by Bishop et al. (2015, 2016). The Voronoi structure is first created within a bounding box of the tube. This structure is then projected through voxelation (direct injection) onto the underlying finite element mesh. Figure 6 shows the tube example with the voxelated Voronoi microstructure imprinted on the finite element mesh. There are 51,750 grains with approximately four grains through the thickness of the tube. For the finite element discretisation described in Subsection 5.3, there are 32 finite elements through the thickness of the tube. Thus, there are approximately eight finite elements per grain dimension. Note that this Voronoi-based microstructure is obtained using a stochastic process, and is thus just one realisation.

For infinitesimally small grain sizes, the equiaxed Voronoi microstructure is statistically homogeneous and can be homogenised using standard techniques (Bishop et al., 2015). If there is no preferred orientation in the crystalline grains (no texture), then the homogeneous material is isotropic. For the given stainless steel austenitic grains, the homogenised material has a Young's modulus $E = 197.5$GPa and a Poisson's ratio $v = 0.294$ (Bishop et al., 2015). For the given tube example with only four grains through the thickness of the tube, the assumption of infinitesimally small grains relative to the structural length scale is clearly violated.

5.2.2 *AM microstructure*

The second microstructure results from a simulated laser-based additive-manufacturing process known as LENS (Griffith et al., 1996; Adams et al., 2019). An example microstructure representing AM materials produced by the LENS process is shown in Figure 1. This microstructure is obtained through a KMC model as described by Rodgers et al. (2018). The KMC model simulates grain growth through a Monte-Carlo process

with a time-varying temperature field as input. The KMC model uses a rectilinear structured grid and typically assumes an idealised double-ellipsoid-based heat source to represent the laser moving across the material. The resulting grain structure is mapped to the finite element mesh of the tube using a direct insertion (voxelation). Figure 7 shows the tube example with the voxelated LENS/KMC microstructure imprinted on the finite element mesh. There are 29,949 grains. Note that this KMC-based microstructure is obtained using a stochastic process and is thus just one realisation as with the Voronoi microstructure.

Figure 7   Tube with imprinted grain structure resulting from a KMC simulation of the LENS metal additive-manufacturing process (see online version for colours)
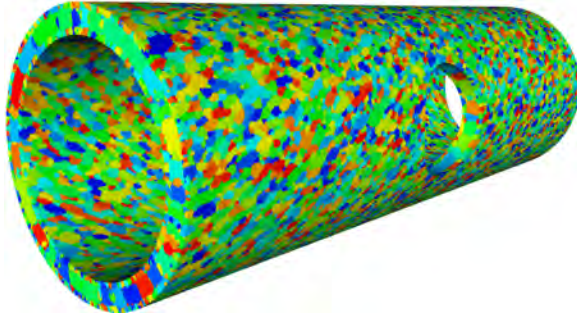
Notes: The tube is built up circumferentially using two laser passes per layer. The number of grains is 29,949 (grain colouring is random).

Figure 8   von Mises stress field of the tube with embedded equiaxed microstructure (Voronoi) subjected to uniaxial tractions (units are MPa) (see online version for colours)
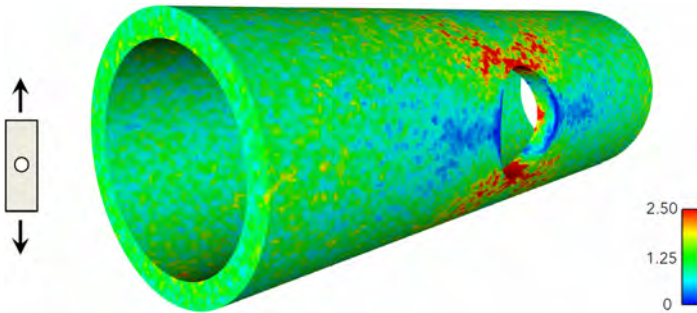
Figures 8 and 9 show the *exact* fine-scale von Mises stress field for the tubes with embedded equiaxed (Voronoi) and AM (KMC) microstructures, respectively. The fine-scale stress fluctuation is apparent and distinctly different between these two microstructures. These results can be compared with the homogeneous isotropic solution given in Figure 5 in which the fine-scale stress fluctuations are effectively filtered out. The differences are more apparent in the side view of the tubes shown in Figure 10. For simplicity, the full finite element mesh of the tube with 29.8 M elements was used for all three cases including the homogeneous case. Of course, in practice a much coarser mesh

would be used for the homogeneous case. Since these microstructures are obtained using a stochastic process, these stress fields represent just one realisation of a random field. Figure 11 shows a linear trace of the von Mises stress along the outside of the tube, midway between the holes ($x = 0$, $y = 5$) for both microstructures. Results for three realisations are given along with the homogeneous isotropic solution. The stress fluctuations are similar between the two types of microstructures, although greater variations are seen for the AM microstructure. The homogeneous isotropic solution provides a reasonable approximation of the local mean behaviour.

Figure 9 von Mises stress field of the tube with embedded AM microstructure (KMC) subjected to uniaxial tractions (units are MPa) (see online version for colours)
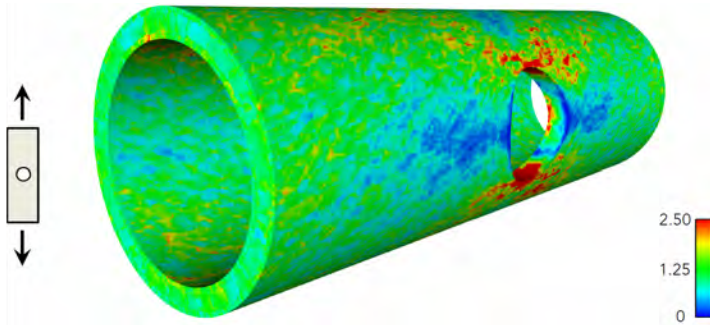

Figure 10 Comparison of the von Mises stress fields of the tube subjected to uniaxial tractions, (a) homogeneous and isotropic material (b) embedded equiaxed microstructure (wrought) (c) AM microstructure (units are MPa) (see online version for colours)
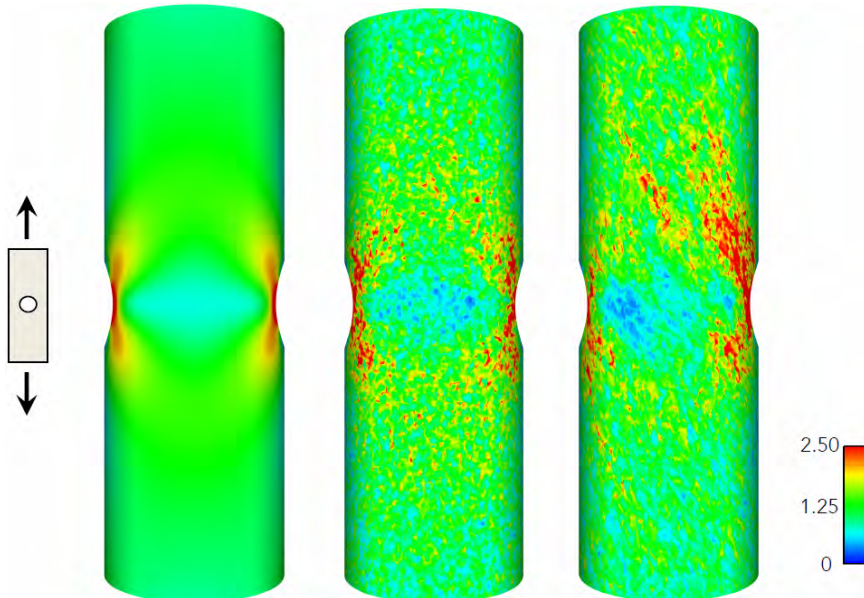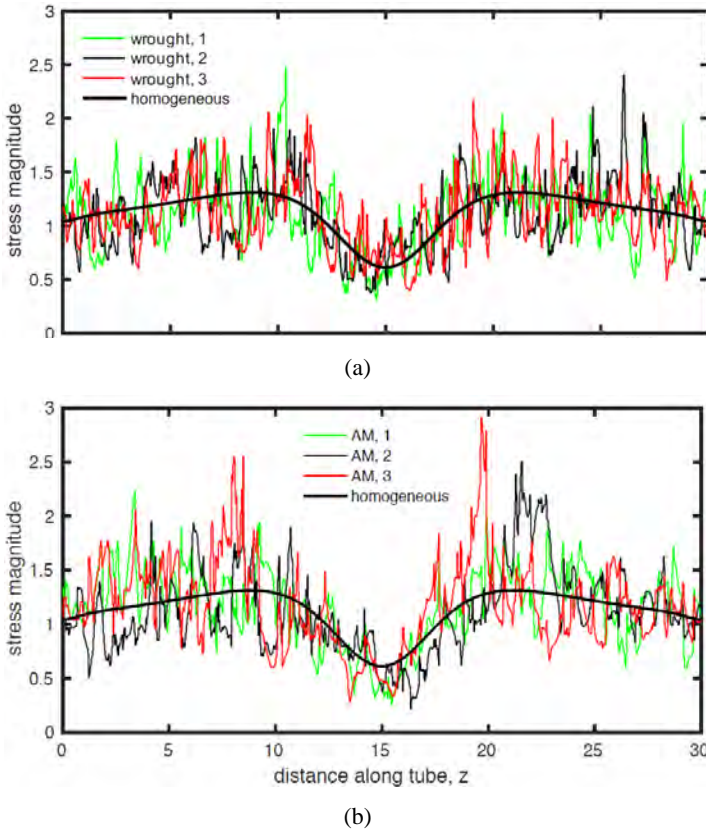
Figure 11 Comparison of the von Mises stress fields of the tube along a linear trace (*z* direction) on the outside of the tube, midway between the holes (*x* = 0, *y* = 5), (a) embedded equiaxed microstructure (wrought) (b) AM microstructure (see online version for colours)

(a)

(b)

Notes: Three realisations of each microstructure are given along with the homogeneous and isotropic solution (stress units are MPa).

Figure 12 (a) Partition of the tube into 904 subdomains (random colours) (b) Finite element mesh of one subdomain consisting of 8^5 = 32,768 hexahedral elements (c) Subdomain with imprinted (voxelated) equiaxed grain structure shown in Figure 6 (see online version for colours)
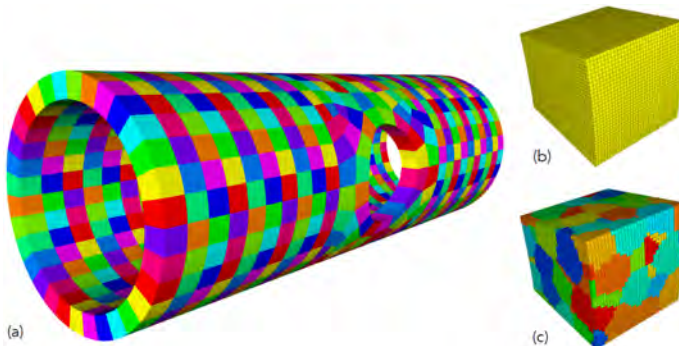
5.3   Domain partition

In this section we discuss the partition of the tube domain into subdomains and subsequent assembly into patches as described in Section 4 for use in the fine-scale recovery process given an approximate macroscale solution. Taking advantage of symmetry, the tube was first sectioned along the three symmetry planes into eight equal subpieces. A coarse hexahedral mesh was constructed for one of these octants consisting of 113 elements. This mesh was then reflected to construct the full mesh of the tube consisting of 904 elements. This initial mesh provided the structure of the partition of the domain. This coarse mesh was subsequently refined hierarchically using a 1-to-8 uniform refinement strategy. After each mesh refinement, surface nodes were projected back to the surface of the tube. After five refinements, each subdomain contained $8^5 = 32{,}768$ finite elements. The total fine-scale mesh consisted of 29.8 M elements and is the same mesh that was used to obtain the 'exact' fine-scale solutions shown in Figures 8 and 9. The resulting partition is shown in Figure 12(a). The fine-scale mesh of one subdomain in shown in Figure 12(b) along with the imprinted equiaxed grain structure (Voronoi) in Figure 12(c).

Table 1   Number of patches for each step in the *type-2* fine-scale recovery sequence obtained using the greedy colouring algorithm

Step	1	2	3	4	5	6
Number of patches	236	220	236	210	32	16

Note: The length of the sequence is six (colours), and the total number of patches is 950.

Table 2   Number of patches for each step in the *type-3* fine-scale recovery sequence obtained using the greedy colouring algorithm

Step	1	2	3	4	5	6	7	8	9	10	11	12	13	14	15	16
Num.	96	92	92	90	92	88	85	78	77	43	29	26	10	3	2	1

Note: The length of the sequence is 16 (colours), and the total number of patches is 904.

For the type-1 fine-scale recovery sequence, the patches are simply the subdomains themselves. The boundary-value problem for each patch then can be solved independently. This is the original HDPM method proposed by Zohdi et al. (1996). For type-2 fine-scale recovery, the total number of patches is 950. This number does not differ much from the number of subdomains (904). This is due to the nature of the partition of the tube, which for the given number of subdomains, is two-dimensional in nature and surface dominated. A finer partition of the tube would be three dimensional in nature and volume dominated. Since type-2 recovery is based on subdomains attached to vertices of the initial decomposition, each patch consists of approximately four subdomains, except near the boundary. The greedy colouring algorithm results in a recovery sequence consisting of six sets of patches. The number of patches for each step in the sequence is given in Table 1. For type-3 fine-scale recovery, again the total number of patches is the same as the number of subdomains, since each patch is based on subdomains attached to a given subdomain. The greedy colouring algorithm results in recovery sequence consisting of 16 sets of patches. The number of patches for each step in the sequence is given in Table 2.

5.4   Fine-scale recovery and exact error

In this section, we recover the approximate fine-scale solution using the three recovery methods, given the approximate macroscale solution obtained using the homogeneous isotropic material (Figure 5). The recovered approximate stress fields are then compared with the exact solution computed from direct numerical simulation to obtain the exact error. Figure 13 shows the recovered von Mises stress field using the three recovery methods for the tube with equiaxed microstructure. The exact stress field shown in Figure 8 is shown again here for comparison. The stress fields for the type-2 and type-3 recovery methods are nearly indistinguishable and very similar to the exact stress field. Note that the type-1 recovered stress field exhibits significant stress noise at the subdomain boundaries. Figure 14 shows the recovered von Mises stress field using the three recovery methods for the tube with AM microstructure. Unlike for the equiaxed microstructure, the stress fields for each recovery method are distinctly different and significantly different than the exact stress field. Again, the type-1 recovered stress field exhibits significant stress noise at the subdomain boundaries.

Figure 13   von Mises stress field for the tube example with equiaxed microstructure, (a) approximate macroscale stress field using a homogeneous isotropic material (b) (c) (d) fine-scale stress fields recovered from Figure 13(a) (e) exact stress field computed by direct numerical simulation of the full microstructure (units are MPa) (see online version for colours)

(a) homogeneous   (b) type 1   (c) type 2   (d) type 3   (e) exact
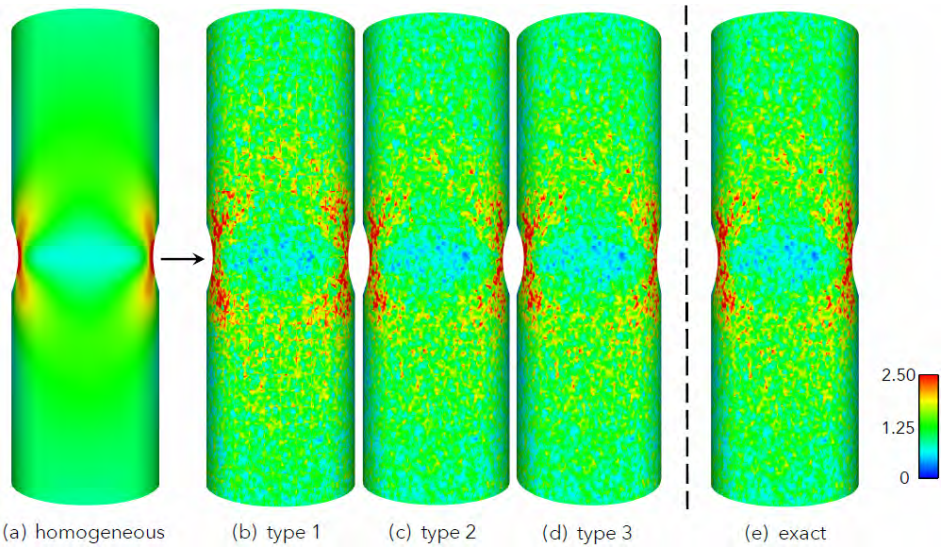
Figure 15 shows the magnitude of the stress error $\|\boldsymbol{\sigma} - \boldsymbol{\sigma}^{ex}\|$ using the three recovery methods for the tube with equiaxed microstructure. Note that a smaller scale is used for type-2 and type-3 recovery methods in order to show more detail. The stress error for the type-2 and type-3 recovery methods is significantly less than that for the type-1 recovery method. The stress error for type-3 recovery is less than the error to type-2 recovery. For the type-1 recovery, there is significant stress error along the subdomain boundaries. The stress error at the patch boundaries is much less apparent for the type-2 and type-3 recovery methods.

Figure 14 von Mises stress field for the tube example with AM microstructure, (a) approximate macroscale stress field using a homogeneous isotropic material (b) (c) (d) fine-scale stress fields recovered from Figure 14(a) (e) exact stress field computed by direct numerical simulation of the full microsctructure (units are MPa) (see online version for colours)


(a) homogeneous (b) type 1 (c) type 2 (d) type 3 (e) exact

Figure 15 Local exact stress error (magnitude) for the tube example with equiaxed microstructure for each of the three fine-scale recovery methods (units are MPa) (see online version for colours)

(a) type 1 (b) type 2 (c) type 3

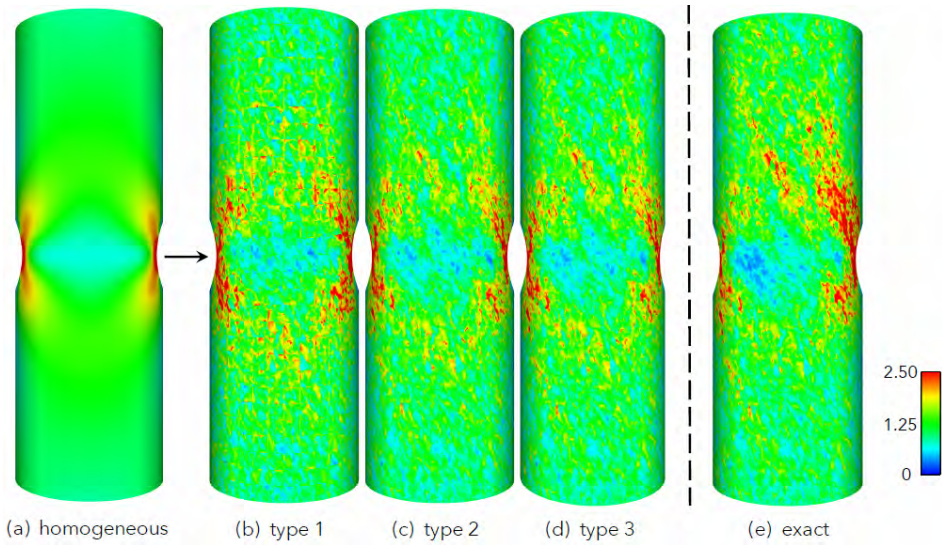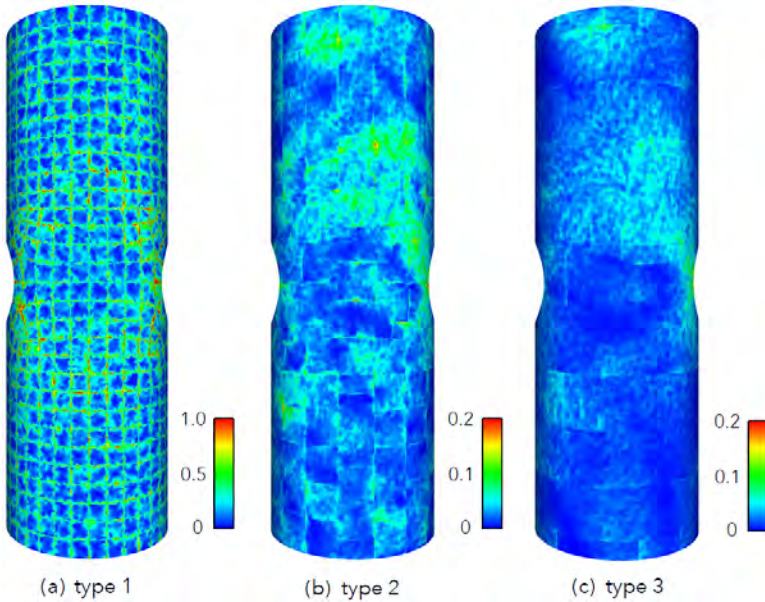Note: The smaller scales used for type-2 and type-3 recovery.

Figure 16   Local exact stress error (magnitude) for the tube example with AM microstructure for each of the three fine-scale recovery methods (units are MPa) (see online version for colours)
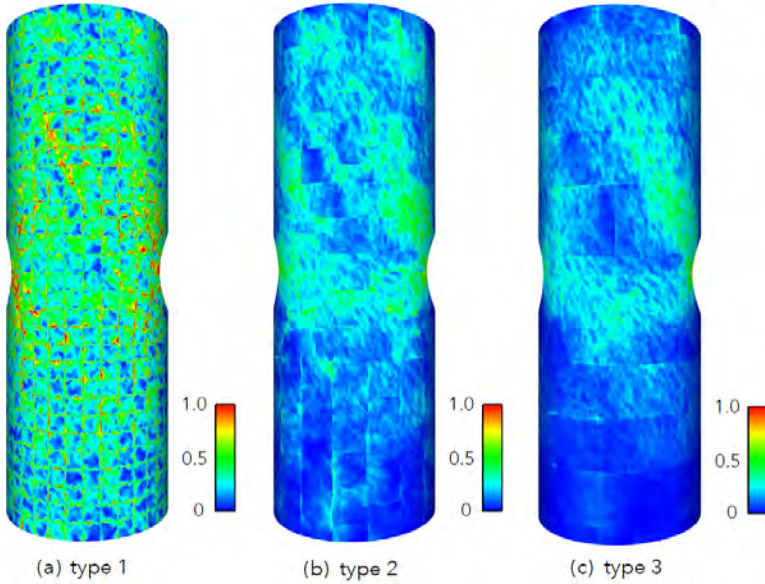

(a) type 1   (b) type 2   (c) type 3

Table 3   Error norms for the tube with equiaxed microstructure for each fine-scale recovery method

Recovery type	$\|\sigma\|_{\Omega}$	$\|\epsilon\|_{\Omega}$	$\dfrac{\|\boldsymbol{\sigma}-\boldsymbol{\sigma}^{\mathrm{ex}}\|_{\Omega}}{\|\boldsymbol{\sigma}^{\mathrm{ex}}\|_{\Omega}}$	$\dfrac{\|\boldsymbol{\epsilon}-\boldsymbol{\epsilon}^{\mathrm{ex}}\|_{\Omega}}{\|\boldsymbol{\epsilon}^{\mathrm{ex}}\|_{\Omega}}$	$\dfrac{\|\mathbf{w}-\mathbf{u}\|_{E}}{\|\mathbf{u}\|_{E}}$
Exact	34.6	1.96×10^{-4}	–	–	–
Homogeneous	32.1	1.76×10^{-4}	0.37	0.40	0.28
Type-1	35.7	1.87×10^{-4}	0.21	0.22	0.15
Type-2	34.1	1.92×10^{-4}	0.029	0.031	0.021
Type-3	34.1	1.96×10^{-4}	0.20	0.021	0.014

Notes: Results are also given for the homogeneous isotropic solution. Values are
   normalised by the exact value (**w** is a recovered fine-scale solution).

Figure 16 shows the magnitude of the stress error using the three recovery methods for the tube with AM microstructure. As with the equiaxed case, the stress error is significantly less for the type-2 and type-3 recovery methods. Also, the stress error for type-3 recovery is less than the error to type-2 recovery. The stress error at the patch boundaries is less apparent for type-2 recovery and much less so for type-3 recovery. In general, the stress error is greater for the additive microstructure compared to the wrought microstructure. This observation is consistent with the fact that the approximate macroscale solution is using the true homogenised material properties for the equiaxed microstructure. But, the homogenised material properties are obtained in the limit of infinitesimal microstructure. Since the grain structure in the tube is relatively large (four grains through the tube thickness), this result demonstrates errors induced when the length scale of the microstructure approaches the characteristic length scale of the structure itself.

Figure 17 Local exact error in the energy norm (squared) for the tube example with equiaxed microstructure for each of the three fine-scale recovery methods (units are MPa) (see online version for colours)

(a) type 1   (b) type 2   (c) type 3
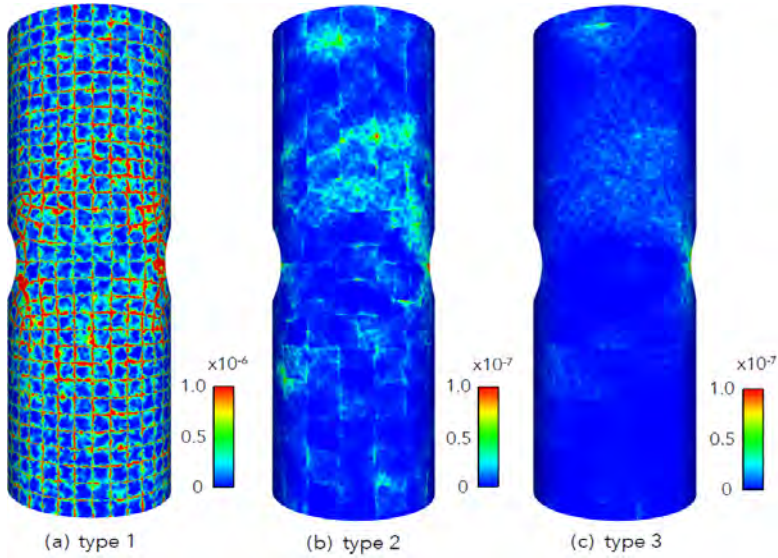
Notes: The scale used for type-2 and type-3 recovery is an order of magnitude less than that used for the type-1 recovery.

Figure 18 Local exact error in the energy norm (squared) for the tube example with AM microstructure for each of the three fine-scale recovery methods (units are MPa) (see online version for colours)

(a) type 1   (b) type 2   (c) type 3
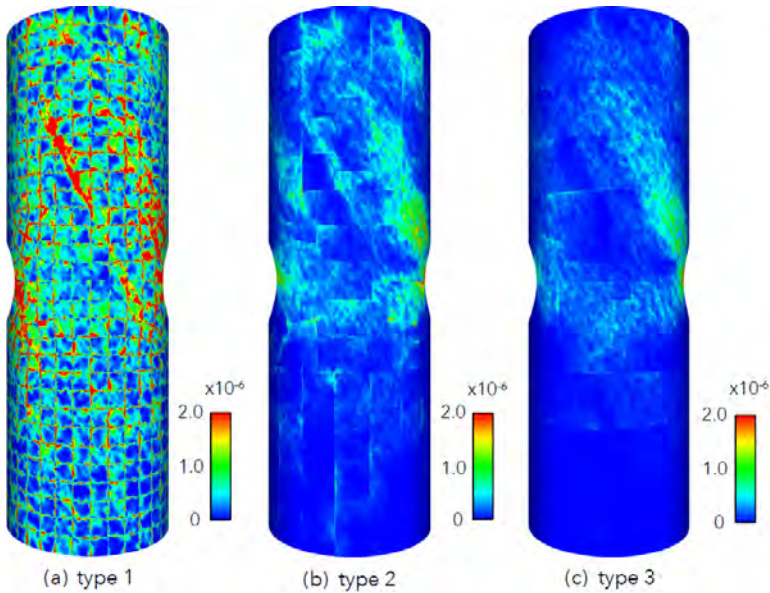
Figures 17 and 18 shows the exact local error in the energy norm (squared) for the equiaxed and AM microstructures, respectively. Note that a smaller scale is used in Figure 17 for type-2 and type-3 recovery methods in order to show more detail. For both cases, the error is greater for the type-1 recovery method than the type-2 and type-3 recovery methods. In general, the error is greater for the additive microstructure compared to the wrought microstructure.

The global norms of the exact error in stress and strain are summarised in Tables 3 and 4 for the equiaxed and AM microstructures, respectively, for each of the three recovery methods. The exact error in the energy norm is also given. The errors are normalised by the exact values of each quantity of interest (e.g., the global norm of the exact stress field). Each error decrease monotonically progressing from type-1 to type-3 recovery methods. The error is greater for the AM microstructure than the wrought microstructure for each recovery method. These results for the global error norms are consistent with the local spatial variations shown in the previous figures.

Table 4   Error norms for the tube with AM microstructure for each fine-scale recovery method

Recovery type	$\|\sigma\|_\Omega$	$\|\epsilon\|_\Omega$	$\dfrac{\|\sigma - \sigma^{\mathrm{ex}}\|_\Omega}{\|\sigma^{\mathrm{ex}}\|_\Omega}$	$\dfrac{\|\epsilon - \epsilon^{\mathrm{ex}}\|_\Omega}{\|\epsilon^{\mathrm{ex}}\|_\Omega}$	$\dfrac{\|\mathbf{w} - \mathbf{u}\|_E}{\|\mathbf{u}\|_E}$
Exact	34.3	2.04×10^{-4}	–	–	–
Homogeneous	32.1	1.76×10^{-4}	0.35	0.44	0.30
Type-1	36.9	1.84×10^{-4}	0.30	0.33	0.22
Type-2	34.0	1.94×10^{-4}	0.13	0.14	0.096
Type-3	33.7	1.96×10^{-4}	0.10	0.11	0.072

Notes: Results are also given for the homogeneous isotropic solution. Values are
        normalised by the exact value ($\mathbf{w}$ is a recovered fine-scale solution).

5.5   *Error bound in the energy norm*

Tables 5 and 6 give the multiscale error bound ψ in the energy norm defined in equation (32), for the equiaxed and AM microstructures, respectively, for each fine-scale recovery method. The exact error in the energy norm $\|\mathbf{w} - \mathbf{u}\|_E$ is given as well. The contributions Z and β to ψ are also given. Recall that Z is the coarse-scale error bound and depends only upon the coarse-scale approximate solution and the fine-scale material properties, while β is the contribution from the fine-scale recovery acting to decrease the error bound. The bound ψ decreases by approximately 15 to 30% when including the effect of the recovered fine-scale solution w, with the greatest decrease when using the type-2 and type-3 recovery methods. There is little difference between the bound ψ using the type-2 and type-3 recovery methods for the wrought microstructure, unlike for the additive microstructure. It is interesting that the bound ψ is similar between the two microstructures for the type-2 and type-3 recovery methods, but the exact error is much smaller for the wrought microstructure. Unfortunately, there is not a clear local-error indicator for multiscale bound ψ, unlike for the coarse-scale bound Z.

Finally, note that the presented results for the tube example are for one realisation of the microstructures, both equiaxed and AM. The error estimation process could be repeated for a large number of microstructural realisations to build up statistical bounds as noted in Romkes et al. (2006) and performed for idealised AM microstructures with

property variations that could be represented at the coarse scale by Brown and Bishop (2019).

Table 5 Multiscale model-form error bound ψ for the wrought microstructure for each fine-scale recovery method

Recovery type	Z^2	β^2	ψ	$\|\mathbf{w} - \mathbf{u}\|_E$
Homogeneous	2.00×10^{-3}	–	0.0447	0.0289
Type-1	2.00×10^{-3}	6.38×10^{-4}	0.0369	0.0156
Type-2	2.00×10^{-3}	8.69×10^{-4}	0.0336	0.00219
Type-3	2.00×10^{-3}	8.64×10^{-4}	0.0337	0.00146

Notes: The contributions Z and β to ψ are also given, with $\psi^2 = Z^2 - \beta^2$ from equation (32). The exact error $\|\mathbf{w} - \mathbf{u}\|_E$ is also provided.

Table 6 Multiscale model-form error bound ψ for the AM microstructure for each fine-scale recovery method

Recovery type	Z^2	β^2	ψ	$\|\mathbf{w} - \mathbf{u}\|_E$
Homogeneous	1.98×10^{-3}	–	0.0445	0.0316
Type-1	1.98×10^{-3}	4.91×10^{-4}	0.0386	0.0232
Type-2	1.98×10^{-3}	9.35×10^{-4}	0.0323	0.00992
Type-3	1.98×10^{-3}	9.79×10^{-4}	0.0316	0.00747

Notes: The contributions Z and β to ψ are also given, with $\psi^2 = Z^2 - \beta^2$ from equation (32). The exact error $\|\mathbf{w} - \mathbf{u}\|_E$ is also provided.

6 Macroscale material model adaptivity

A goal of *a posteriori* estimation of *discretisation* error is to not only estimate the error but to also reduce it through adaptation of the discretisation. Similarly, for *a posteriori* estimation of model-form error, we seek to reduce the error by adapting the physical model. For the present case of multiscale structural modelling, we can adapt the physical model in several ways. One approach to reducing *model-form* error is to directly embed the fine-scale microstructure in the macroscale model in locations in which the local-error indicator ζ^2 is relatively large as proposed by Oden and Zohdi (1997), Oden and Vemaganti (1999, 2000), Vemaganti and Oden (2001) and Chamoin and Legoll (2021). Alternatively, we can adapt the approximate material model by adjusting the local material parameters as proposed by Bishop and Brown (2018) for the single-scale case. In that work, the local material parameters were adapted in post-processing step by assuming either a strain-fixed or stress-fixed state and then solving for local material parameters that minimised the local-error indicator ζ^2. Here, we adopt a similar approach in that we adapt the approximate macroscale material parameters, but instead of using the error estimates ζ^2 or ψ^2 we use local averages of the recovered fine-scale solution. The local macroscale parameters that relate the locally averaged stress and strain values are then chosen to reduce the constitutive modelling error.

There are several possibilities for obtaining a locally averaged stress or strain field including the use of a convolution as explored by Bishop et al. (2015). Here, we simply average the recovered fine-scale fields over the subdomains Ω_M within the domain

partition (Subsection 5.3). The mean stress $\bar{\boldsymbol{\sigma}}_M$ and mean strain $\bar{\epsilon}_M$ tensors are defined as

$$\bar{\boldsymbol{\sigma}}_M := \frac{1}{V_M} \int_{\Omega_M} \boldsymbol{\sigma} \, d\Omega \text{ and } \bar{\epsilon}_M := \frac{1}{V_M} \int_{\Omega_M} \epsilon \, d\Omega \tag{34}$$

where $\boldsymbol{\sigma}$ and $\bar{\epsilon}$ are the recovered approximate fine-scale stress and strain tensors, respectively, and V_M is the volume of the averaging domain Ω_M.

We then search for macroscale material parameters that minimise the constitutive relationship between the mean stress $\bar{\boldsymbol{\sigma}}_M$ and the mean strain $\bar{\epsilon}_M$ tensors. For the case of elasticity, we search for an optimal elasticity tensor $\mathbb{C}_M$ in each local region by minimising an appropriate error functional. There are several possible error functionals. For example, we can minimise the squared norm of the difference between $\bar{\boldsymbol{\sigma}}_M$ and $\mathbb{C}_M$ times $\bar{\epsilon}_M$, denoted by F^σ,

$$F^\sigma := \left\| \bar{\boldsymbol{\sigma}}_M - \mathbb{C}_M \bar{\epsilon}_M \right\|^2. \tag{35}$$

Conversely, we can minimise the squared norm of the difference between $\bar{\epsilon}_M$ and $\mathbb{S}_M$ times $\bar{\boldsymbol{\sigma}}_M$, denoted by F^ϵ,

$$F^\epsilon := \left\| \bar{\epsilon}_M - \mathbb{S}_M \bar{\boldsymbol{\sigma}}_M \right\|^2. \tag{36}$$

We can also minimise the strain energy of the stress and strain difference, denoted by F^W,

$$F^W := \left(\bar{\boldsymbol{\sigma}}_M - \mathbb{C}_M \bar{\epsilon}_M \right) : \left(\bar{\epsilon}_M - \mathbb{S}_M \bar{\boldsymbol{\sigma}}_M \right). \tag{37}$$

For each of these error functionals, the optimal stiffness tensor, $\mathbb{C}_M^{opt}$ is given by

$$\mathbb{C}_M^{opt} := \underset{\mathbb{C}_M \in \mathcal{C}}{\arg \min} \, F \tag{38}$$

where F is one of the three error functionals, and $\mathcal{C}$ is the vector subspace of possible stiffness tensors. Note that this optimisation process does not involve the exact solution of the fine-scale problem.

In general, $\mathcal{C}$ includes anisotropic stiffness tensors. For simplicity, we choose $\mathcal{C}$ to be the space of isotropic stiffness tensors. Thus, from equation (4), we can write any $\mathbb{C} \in \mathcal{C}$ in the form

$$\mathbb{C} = a\mathbb{J} + b\mathbb{K} \tag{39}$$

where $a = 3K$ and $b = 2\mu$. Here, K and μ are the *apparent* bulk and shear moduli, respectively, since they depend on the given boundary value problem. Also, from equation (7)

$$\mathbb{S} = \frac{1}{a}\mathbb{J} + \frac{1}{b}\mathbb{K}. \tag{40}$$

Necessary conditions for a local extremum in the error functionals are provided by

$$\frac{\partial F}{\partial a} = 0 \text{ and } \frac{\partial F}{\partial b} = 0. \tag{41}$$

Since the error functionals are quadratic in a and b, we can derive explicit expressions for a and b, and thus K_M and μ_M. These expressions are given in the following subsections for each error functional. We omit the subscript M for these derivations for clarity.

6.1 Optimal $\mathbb{C}_M$ using F^σ

We show the derivation of the optimal macroscale material parameters using the error functional F^σ. Substituting equation (35) into equation (41) (a) gives

$$(\overline{\boldsymbol{\sigma}} - \mathbb{C}\overline{\boldsymbol{\epsilon}}) : \left(\frac{\mathbb{C}}{\partial a}\overline{\boldsymbol{\epsilon}}\right) = 0. \tag{42}$$

From equation (39), $\partial\mathbb{C}/\partial a = \mathbb{J}$ so that $(\overline{\boldsymbol{\sigma}} - (a\mathbb{J} + b\mathbb{K})\overline{\boldsymbol{\epsilon}}) : (\mathbb{J}\overline{\boldsymbol{\epsilon}}) = 0$. Expanding this equation and noting that $(\mathbb{K}\overline{\boldsymbol{\epsilon}}) : (\mathbb{J}\overline{\boldsymbol{\epsilon}}) = 0$ gives

$$\boxed{a = 3K = \frac{hyd\,(\overline{\boldsymbol{\sigma}})}{hyd\,(\overline{\boldsymbol{\epsilon}})} = \frac{\overline{\sigma}_{kk}}{\overline{\epsilon}_{kk}}} \tag{43}$$

where $hyd(\cdot)$ denotes the hydrostatic part of the given second order tensor. Similarly, substituting equation (35) into equation (41) (b) gives

$$(\overline{\boldsymbol{\sigma}} - \mathbb{C}\overline{\boldsymbol{\epsilon}}) : \left(\frac{\mathbb{C}}{\partial b}\overline{\boldsymbol{\epsilon}}\right) = 0. \tag{44}$$

From equation (39), $\partial\mathbb{C}/\partial b = \mathbb{K}$ so that $(\overline{\boldsymbol{\sigma}} - (a\mathbb{J} + b\mathbb{K})\overline{\boldsymbol{\epsilon}}) : (\mathbb{K}\overline{\boldsymbol{\epsilon}}) = 0$. Expanding this equation results in

$$\boxed{b = 2\mu = \frac{dev\,(\overline{\boldsymbol{\sigma}}) : dev\,(\overline{\boldsymbol{\epsilon}})}{dev\,(\overline{\boldsymbol{\epsilon}}) : dev\,(\overline{\boldsymbol{\epsilon}})} = \frac{\overline{\sigma}_{ij}\overline{\epsilon}_{ij} - \dfrac{1}{3}\overline{\sigma}_{kk}\overline{\epsilon}_{kk}}{\overline{\epsilon}_{ij}\overline{\epsilon}_{ij} - \dfrac{1}{3}\overline{\epsilon}_{kk}^2}} \tag{45}$$

where $dev(\cdot)$ denotes the deviatoric part of the given second order tensor.

6.2 Optimal $\mathbb{C}_M$ using F^ϵ

Using a similar derivation, but with the error functional F^ϵ, we obtain the following expression for the optimal shear modulus,

$$\boxed{2\mu = \frac{dev\,(\overline{\boldsymbol{\sigma}}) : dev\,(\overline{\boldsymbol{\sigma}})}{dev\,(\overline{\boldsymbol{\sigma}}) : dev\,(\overline{\boldsymbol{\epsilon}})} = \frac{\overline{\sigma}_{ij}\overline{\sigma}_{ij} - \dfrac{1}{3}\overline{\sigma}_{kk}^2}{\overline{\sigma}_{ij}\overline{\epsilon}_{ij} - \dfrac{1}{3}\overline{\sigma}_{kk}\overline{\epsilon}_{kk}}.} \tag{46}$$

The result for optimal bulk modulus is the same as equation (43).

Figure 19   Variation of the adapted shear modulus for the tube with equiaxed microstructure
obtained by minimising the energy functional F^W for each of the three fine-scale
recovery methods (units are GPa), (a) type 1 (b) type 2 (c) type 3 (see online version
for colours)

(a)   (b)   (c)
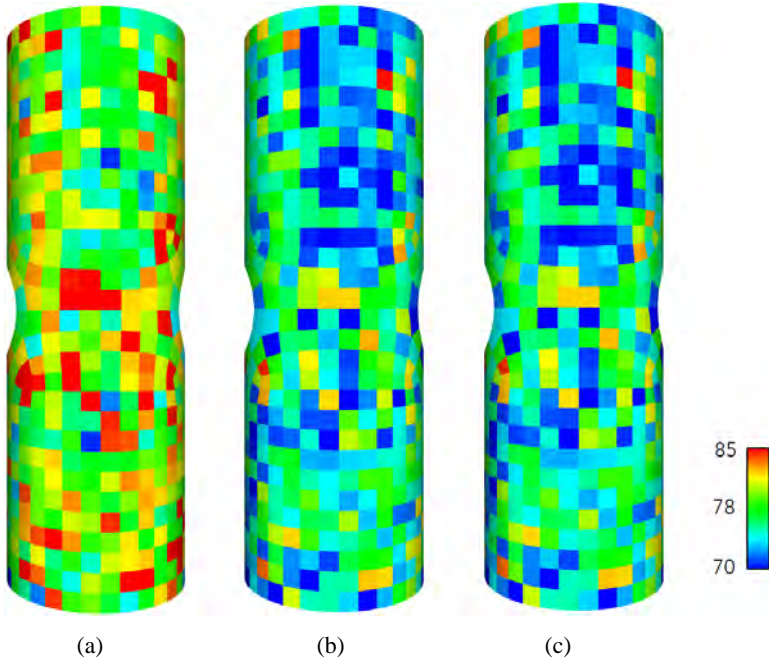
Note: For reference, the homogenised shear modulus obtained for a statistically
homogeneous and isotropic microstructure is 76.4 GPa.

Source: Bishop et al. (2016)

6.3   Optimal $\mathbb{C}_M$ using F^W

Using a similar derivation, but with the error functional F^W, we obtain the following
expression for the optimal shear modulus,

$$2\mu = \frac{dev(\overline{\boldsymbol{\sigma}}):dev(\overline{\boldsymbol{\sigma}})}{dev(\overline{\boldsymbol{\epsilon}}):dev(\overline{\boldsymbol{\epsilon}})} = \frac{\overline{\sigma}_{ij}\overline{\sigma}_{ij} - \dfrac{1}{3}\overline{\sigma}_{kk}^2}{\overline{\epsilon}_{ij}\overline{\epsilon}_{ij} - \dfrac{1}{3}\overline{\epsilon}_{kk}^2}. \tag{47}$$

The result for optimal bulk modulus is the same as equation (43).

6.4   Tube example

Figure 19 shows the variation in the adapted shear modulus using the energy functional
F^W for the tube example with equiaxed microstructure for each fine-scale recovery
method. The adapted shear modulus for the type-1 recovery method has a range of over
20% of the nominal (homogenised) value of 76.4 GPa obtained for a statistically
homogeneous and isotropic microstructure (Bishop et al., 2016). The observed variation

is smaller for the type-2 and type-3 recovery methods. The adapted shear modulus has little spatial structure due to the relatively small grain structure (see Figure 6) and no texture (uniformly random orientations).

Figure 20 shows the variation in the adapted shear modulus using the energy functional F^W for the tube example with AM microstructure for each fine-scale recovery method. The adapted shear modulus for the type-1 recovery method has a range of over 90% of the nominal (homogenised) value of 76.4 GPa. This variation is somewhat smaller for the type-2 and type-3 recovery methods. Unlike for the equiaxed case, the adapted shear modulus for the AM material has significant spatial patterning due to the relatively large grain sizes (see Figure 7). Larger grains lead to larger spatial areas with similar adaptive properties since the entire area of each (large) grain has the same orientation, and thus the same mechanical behaviour.

Figure 20   Variation of the adapted shear modulus for the tube with AM microstructure obtained by minimising the energy functional F^W for each of the three fine-scale recovery methods (units are GPa), (a) type 1 (b) type 2 (c) type 3 (see online version for colours)

(a)   (b)   (c)
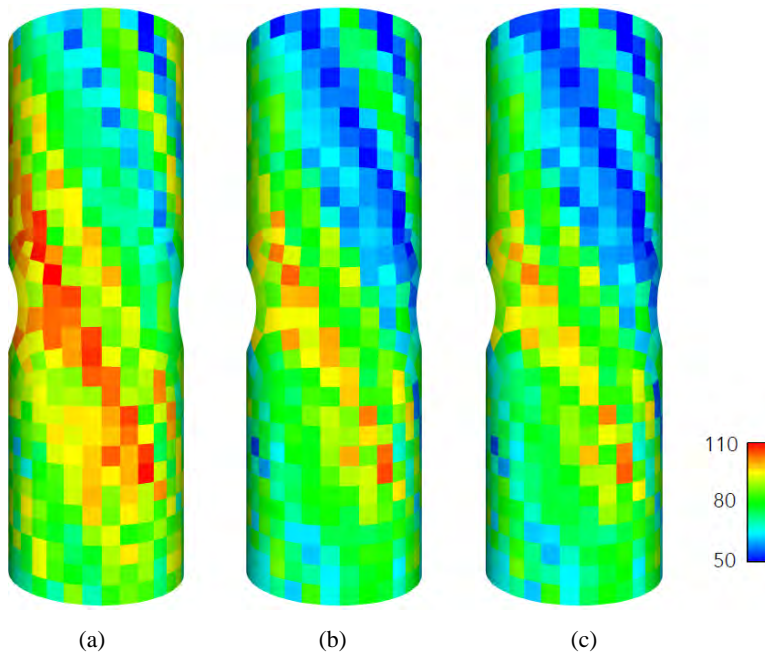
Notes: For reference, the homogenised shear modulus obtained for a statistically homogeneous and isotropic microstructure is 76.4 GPa (the difference in scale compared to Figure 19).

   Source: Bishop et al. (2016)

Results for the adapted shear modulus using the energy functionals F^σ and F^ϵ are similar and are not shown. Interestingly, since the grains in the example microstructures have a cubic symmetry, the bulk modulus is spatially uniform (constant) for all possible microstructures. It follows that the mean of the hydrostatic stress and strain over each subdomain is constant throughout the domain. Thus, the use of equation (43) results in no change of value. However, since Young's modulus and Poisson's ratio are nonlinear

functions of μ, their adapted values will both vary spatially. Note again that the adapted values are not material properties *per se*, but will depend on the given boundary-value problem. Indeed, a highly textured microstructure with anisotropic effective behaviour would result in adaptive isotropic properties with much more spatial dependence (Bishop and Brown, 2018).

Finally, the updated material parameters could be used in an iterative scheme to reduce the model-form error as reported in Bishop and Brown (2018) for the single-scale case. For the examples considered there, the material parameters were observed to converge very quickly. This will not be explored here, however.

7   Summary

In this work, a multiscale error-estimation methodology was investigated for assessing the model-form error in the energy norm for elastic deformations in both wrought and AM steel structures. An approximate macroscale (coarse scale) solution was used to recover an approximate fine-scale solution. The recovered fine-scale solution was then used to calculate quantitative bounds on model-form error in the energy norm. Three methods were investigated for recovering the approximate fine-scale field, given the coarse-scale approximate solution. The first method consisted of a direct projection using non-overlapping subdomains, while the second and third methods involved using a sequence of overlapping patches differing in the degree of overlap. An example of the error-estimation methodology was presented for an AM metallic structure consisting of a highly non-uniform polycrystalline microstructure. A traditional wrought microstructure with equiaxed grains was also used for comparison. The two recovery methods that used overlapping patches were found to be superior to the one recovery method using non-overlapping patches, but little difference was seen between the two overlapping-patch recovery methods. For the wrought microstructure, the error of the solution in the energy norm was reduced by a factor of ten when using the overlapping-patch recovery methods compared to the error when using the non-overlapping patch recovery. For the AM microstructure, the error of the solution in the energy norm was only reduced by a factor of two to three when using the overlapping-patch recovery methods compared to the error when using the non-overlapping patch recovery. A methodology was also proposed for locally adapting the approximate macroscale material parameters to reduce the modelling error. The locally adapted shear modulus was seen to be much more structured for the AM microstructure compared to the wrought microstructure and exhibited larger variations in magnitude.

Acknowledgements

might be expressed in the paper do not necessarily represent the views of the US Department of Energy or the US Government.

References

Abaqus (2021) *Abaqus, Version 2021x* [online] https://www.3ds.com/products-services/simulia/products/abaqus/ (access 1 May 2021).

Adams, D., Reedlunn, B., Maguire, M., Song, B., Carroll, J., Bishop, J., Wise, J., Kilgo, A., Palmer, T., Brown, D. and Clausen, B. (2019) *Mechanical Response of Additively Manufactured Stainless Steel 304L Across A Wide Range of Loading Conditions*, Sandia Report, SAND2019-7001, Sandia National Laboratories, Albuquerque, NM and Livermore, CA.

Ainsworth, M. and Oden, J. (2011) *A Posteriori Error Estimation in Finite Element Analysis*, John Wiley & Sons, New York.

Antonysamy, A., Meyer, J. and Prangnell, P. (2013) 'Effect of build geometry on the β-grain structure and texture in additive manufacturing of Ti-6Al-4V by selective electron beam melting', *Materials Characterization*, Vol. 84, pp.153–168.

Auriault, J. and Bonnet, G. (1987) 'Surface effects in composite materials: two simple examples', *International Journal of Engineering Science*, Vol. 25, No. 3, pp.307–323.

Bensoussan, A., Lions, J. and Papanicolaou, G. (2011) *Asymptotic Analysis for Periodic Structures*, American Mathematical Society.

Bishop, J. and Brown, J. (2018) 'Adaptive reduction of constitutive model-form error using a posteriori error estimation techniques', *CMAME*, Vol. 340, pp.577–599.

Bishop, J. and Lim, H. (2016) 'Continuum approximations', in Weinberger, R. and Tucker, J. (Eds.): *Multiscale Materials Modeling for Nanomechanics*, Chapter 3, Springer International Publishing, Switzerland.

Bishop, J., Emery, J., Battaile, C., Littlewood, D. and Baines, A. (2016) 'Direct numerical simulations in solid mechanics for quantifying the macroscale effects of microstructure and material model-form error', *TMS Journal of Materials*, Vol. 68, No. 5, pp.1427–1445.

Bishop, J., Emery, J., Field, R., Weinberger, C. and Littlewood, D. (2015) 'Direct numerical simulations in solid mechanics for understanding the macroscale effects of microscale material variability', *Computer Methods in Applied Mechanics and Engineering*, Vol. 287, pp.262–289.

Bonet, J. and Wood, R. (2008) *Nonlinear Continuum Mechanics for Finite Element Analysis*, 2nd ed., Cambridge University Press, Cambridge, UK.

Bouche, G., Bechade, J., Mathon, M., Allais, L., Gourgues, A. and Naze, L. (2000) 'Texture of welded joints of 316L stainless steel, multi-scale orientation analysis of a weld metal deposit', *Journal of Nuclear Materials*, Vol. 277, pp.91–98.

Boutin, C. (1996) 'Microstructural effects in elastic composites', *IJSS*, Vol. 33, No. 7, pp.1023–1051.

Bower, A. (2010) *Applied Mechanics of Solids*, Chapter 3.2.16, CRC Press, New York.

Briggs, W., Henson, V.E. and McCormick, S. (2000) *A Multigrid Tutorial*, 2nd ed., SIAM, Philadelphia, PA.

Brown, J. and Bishop, J. (2019) 'Modeling mechanical behavior of an additively manufactured metal structure with local texture variations: a study on model form error', *MSMSE*, Vol. 27, No. 40, p.25003.

Chamoin, L. and Legoll, F. (2021) 'Goal-oriented error estimation and adaptivity in MSFEM computations', *Computational Mechanics*, Vol. 67, No. 4, pp.1201–1228.

Chen, J., Hillman, M. and Chi, S. (2017) 'Meshfree methods: progress made after 20 years', *JEM*, Vol. 143, No. 4, p.4017001.

Christensen, R. (2005) *Mechanics of Composite Materials*, Dover Publications, Mineola, New York.

Ciarlet, P. (2002) *The Finite Element Method for Elliptic Problems*, SIAM, Philadelphia, PA.

Cioranescu, D. and Donato, P. (1999) *An Introduction to Homogenization*, Oxford University Press, New York.

Cubit (2021) *Coreform Cubit* [online] https://coreform.com/products/coreform-cubit/ (accessed 1 May 2021).

Dehoff, R., Kirka, M., Sames, W., Bilheux, H., Tremsin, A., Lowe, L. and Babu, S. (2015) 'Site specific control of crystallographic grain orientation through electron beam additive manufacturing', *Materials Science and Technology*, Vol. 31, No. 8, pp.931–938.

Denlinger, E., Irwin, J. and Michaleris, P. (2014) 'Thermomechanical modeling of additive manufacturing large parts', *Journal of Manufacturing Science and Engineering*, Vol. 136, No. 61007, pp.1–8.

Dinda, G., Dasgupta, A. and Maxumder, J. (2012) 'Texture control during laser deposition of nickel-based superalloy', *Scripta Materialia*, Vol. 67, No. 5, pp.503–506.

Dolean, V., Jolivet, P. and Nataf, F. (2015) *An Introduction to Domain Decomposition Methods: Algorithms, Theory, and Implementation*, SIAM, Philadelphia, PA.

Dumontet, H. (1987) 'Study of a boundary layer problem in elastic composite materials', *Mathematical Modelling and Numerical Analysis*, Vol. 20, No. 2, pp.265–286.

Efendiev, Y. and Hou, T. (2009) *Multiscale Finite Element Methods*, Springer, New York.

Griffith, M., Keicher, D., Atwood, C., Romero, J., Smugeresky, J., Harwell, L. and Greene, D. (1996) 'Freeform fabrication of metallic components using laser engineered net shaping (LENS)', in *Solid Freeform Fabrication Symposium Proceedings*, Austin, TX, 12–14 August, p.125.

Hendrix, B. and Yu, L. (1998) 'Self-consistent elastic properties for transversely isotropic polycrystals', *Acta Materialia*, Vol. 46, No. 1, pp.127–135.

Huet, C. (1990) 'Application of variational concepts to size effects in elastic heterogeneous bodies', *JMPS*, Vol. 38, No. 6, pp.813–841.

Hughes, T. (2000) *The Finite Element Method: Linear Static and Dynamic Finite Element Analysis*, Dover, New York.

Jikov, V., Kozlov, S. and Oleinik, O. (1994) *Homogenization of Differential Operators and Integral Functionals*, Springer-Verlag, New York.

Johnson, K., Rodgers, T., Underwood, O., Madison, J., Ford, K., Whetten, S., Dagel, D. and Bishop, J. (2018) 'Simulation and experimental comparison of the thermo-mechanical history and 3D microstructure evolution of 304L stainless steel tubes manufactured using LENS', *Computational Mechanics*, Vol. 61, No. 5, pp.559–574.

Kanit, T., Forest, S., Galliet, I., Mounoury, V. and Jeulin, D. (2003) 'Determination of the size of the representative volume element for random composites: statistical and numerical approach', *International Journal of Solids and Structures*, Vol. 40, Nos. 13–14, pp.3647–3679.

Larsson, F. and Runesson, K. (2004) 'Modeling and discretization errors in hyperelasto-(visco) plasticity with a view to hierarchical modeling', *Computer Methods in Applied Mechanics and Engineering*, Vol. 193, Nos. 48–51, pp.5283–5300.

Larsson, F. and Runesson, K. (2006) 'Adaptive computational meso-macro-scale modeling of elastic composites', *Computer Methods in Applied Mechanics and Engineering*, Vol. 195, Nos. 4–6, pp.324–338.

Larsson, F. and Runesson, K. (2008) 'Adaptive bridging of scales in continuum modeling based on error control', *International Journal for Multiscale Computational Engineering*, Vol. 6, No. 4, pp.371–392.

Lebensohn, R. and Tomé, C. (1993) 'A self-consistent anisotropic approach for the simulation of plastic deformation and texture development of polycrystals: application to zirconium alloys', *Acta Metallurgica et Materialia*, Vol. 41, No. 9, pp.2611–2624.

Ledbetter, H. (1984) 'Monocrystal-polycrystal elastic constants of a stainless steel', *Physica Status Solidi A*, Vol. 85, No. 1, pp.89–96.

Lewis, R. (2016) *A Guide to Graph Colouring: Algorithms and Applications*, Springer, New York.

Li, C., Wang, Y., Zhan, H., Han, T., Han, B. and Zhao, W. (2010) 'Three-dimensional finite element analysis of temperatures and stresses in wide-band laser surface melting processing', *Materials and Design*, Vol. 31, No. 7, pp.3366–3373.

Liu, X., Réthoré, J., Baietto, M., Sainsot, P. and Lubrecht, A. (2020) 'An efficient finite element based multigrid method for simulations of the mechanical behavior of heterogeneous materials using CT images', *Computational Mechanics*, Vol. 66, No. 6, pp.1427–1441.

Målqvist, A. and Peterseim, D. (2021) *Numerical Homogenization by Localized Orthogonal Decomposition*, SIAM, Philadelphia, PA.

Markl, M. and Körner, C. (2016) 'Multiscale modeling of powder bed-based additive manufacturing', *Annual Review of Materials Research*, Vol. 46, No. 1, pp.93–123.

Miehe, C. and Bayreuther, C. (2007) 'On multiscale FE analyses of heterogeneous structures: from homogenization to multigrid solvers', *International Journal for Numerical Methods in Engineering*, Vol. 71, No. 10, pp.1135–1180.

Moakher, M. and Norris, A. (2006) 'The closest elastic tensor of arbitrary symmetry to an elasticity tensor of lower symmetry', *Journal of Elasticity*, Vol. 85, No. 3, pp.215–263.

Moës, N., Oden, J. and Zohdi, T. (1998) 'Investigation of the interactions between the numerical and the modeling errors in the homogenized Dirichlet projection method', *Computer Methods in Applied Mechanics and Engineering*, Vol. 159, No. 1, pp.79–101.

Oden, J. and Vemaganti, K. (1999) 'Adaptive hierarchical modeling of heterogeneous structures', *Physica D: Nonlinear Phenomena*, Vol. 133, Nos. 1–4, pp.404–415.

Oden, J. and Vemaganti, K. (2000) 'Estimation of local modeling error and goal-oriented adaptive modeling of heterogeneous materials: I. Error estimates and adaptive algorithms', *Journal of Computational Physics*, Vol. 164, No. 1, pp.22–47.

Oden, J. and Zohdi, T. (1997) 'Analysis and adaptive modeling of highly heterogeneous elastic structures', *Computer Methods in Applied Mechanics and Engineering*, Vol. 148, Nos. 3–4, pp.367–391.

Oden, J., Prudhomme, S., Hammerand, D. and Kuczma, M. (2001) 'Modeling error and adaptivity in nonlinear continuum mechanics', *Computer Methods in Applied Mechanics and Engineering*, Vol. 190, Nos. 49–50, pp.6663–6684.

Oden, J., Vemaganti, K. and Moës, N. (1999) 'Hierarchical modeling of heterogeneous solids', *Computer Methods in Applied Mechanics and Engineering*, Vol. 172, Nos. 1–4, pp.3–25.

Pal, D., Patil, N., Zeng, K. and Stucker, B. (2014) 'An integrated approach to additive manufacturing simulations using physics based, coupled multiscale process modeling', *Journal of Manufacturing Science and Engineering*, Vol. 136, No. 6, pp.61022–61022.

Papanicolaou, G. and Varadhan, S. (1979) 'Boundary value problems with rapidly oscillating random coefficients', *Colloquia Mathematica Societatis J'anos Bolyai*, Vol. 27, pp.835–873.

Parimi, L.A.R., Clark, D. and Attallah, M. (2014) 'Microstructural and texture development in direct laser fabricated IN 718', *Materials Characterization*, Vol. 89, pp.102–111.

Rodgers, T., Bishop, J. and Madison, J. (2018) 'Direct numerical simulation of mechanical response in synthetic additively manufactured microstructures', *Modelling and Simulation in Materials Science and Engineering*, Vol. 26, No. 5, p.55010.

Romkes, A., Oden, J. and Vemaganti, K. (2006) 'Multi-scale goal-oriented adaptive modeling of random heterogeneous materials', *Mechanics of Materials*, Vol. 38, Nos. 8–10, pp.859–872.

Shaw, R., Agelastos, A. and Miller, J. (2017) *Guide to Using Sierra*, Sandia Report, SAND2017-3771, Sandia National Laboratories, Albuquerque, NM and Livermore, CA.

Smith, J., Xiong, W., Yan, W., Lin, S., Cheng, P., Kafka, O., Wagner, G., Cao, J. and Liu, W. (2016) 'Linking process, structure, property, and performance for metal-based additive manufacturing: computational approaches with experimental support', *Computational Mechanics*, Vol. 136, pp.1–28.

Smyshlyaev, V. and Cherednichenko, K. (2000) 'On rigorous derivation of strain gradient effects in the overall behaviour of periodic heterogeneous media', *Journal of the Mechanics and Physics of Solids*, Vol. 48, Nos. 6–7, pp.1325–1357.

Strouboulis, T., Copps, K. and Babüka, I. (2001) 'The generalized finite element method', *CMAME*, Vol. 190, No. 32, pp.4081–4193.

Tang, M. and Pistorius, P. (2017) 'Anisotropic mechanical behavior of AlSi10Mg parts produced by selective laser melting', *TMS Journal of Materials*, Vol. 69, No. 3, pp.516–522.

Torquato, S. (2002) *Random Heterogeneous Materials: Microstructure and Macroscopic Properties*, Springer, New York.

Tran, T., Monchiet, V. and Bonnet, G. (2012) 'A micromechanics-based approach for the derivation of constitutive elastic coefficients of strain-gradientmedia', *IJSS*, Vol. 49, No. 5, pp.783–792.

Unnikrishnan, R., Idury, K.S., Ismail, T., Bhadauria, A., Shekhawat, S., Khatirkar, R. and Sapate, S. (2014) 'Effect of heat input on the microstructure, residual stresses and corrosion resistance of 304L austenitic stainless steel weldments', *Materials Characterization*, Vol. 93, pp.10–23.

Vemaganti, K. and Oden, J. (2001) 'Estimation of local modeling error and goal-oriented adaptive modeling of heterogeneous materials: part II: a computational environment for adaptive modeling of heterogeneous elastic solids', *Computer Methods in Applied Mechanics and Engineering*, Vol. 190, Nos. 46–47, pp.6089–6124.

Wang, H., Wu, P., Tomé, C. and Huang, Y. (2010) 'A finite strain elastic-viscoplastic self-consistent model for polycrystalline materials', *Journal of the Mechanics and Physics of Solids*, Vol. 58, No. 4, pp.594–612.

Wei, H., Elmer, J. and Debroy, T. (2016) 'Origin of grain orientation during solidification of an aluminum alloy', *Acta Materialia*, Vol. 115, pp.123–131.

Yaguchi, M. and Busso, E. (2005) 'On the accuracy of self-consistent elasticity formulations for directionally solidified polycrystal aggregates', *International Journal of Solids and Structures*, Vol. 42, Nos. 3–4, pp.1073–1089.

Yuan, X., Tomita, Y. and Andou, T. (2008) 'A micromechanical approach of nonlocal modeling for media with periodic microstructures', *Mechanics Research Communications*, Vol. 35, Nos. 1–2, pp.126–133.

Yushu, D. and Matouš, K. (2020) 'The image-based multiscale multigrid solver, preconditioner, and reduced order model', *Journal of Computational Physics*, Vol. 406, p.109165.

Zohdi, T. and Wriggers, P. (2008) *An Introduction to Computational Micromechanics*, Springer-Verlag, Berlin, Heidelberg.

Zohdi, T., Oden, J. and Rodin, G. (1996) 'Hierarchical modeling of heterogeneous bodies', *Computer Methods in Applied Mechanics and Engineering*, Vol. 138, Nos. 1–4, pp.273–298.